Bioactive Materials 13 (2022) 269–285

Contents lists available at ScienceDirect

Bioactive Materials

journal homepage: www.keaipublishing.com/en/journals/bioactive-materials

NIR-activated nanosystems with self-modulated bacteria targeting for enhanced biofilm eradication and caries prevention☆

Yunjian Yu [a,1], Yufei Zhang [a,1], Yijie Cheng [a], Yuxia Wang [c,d], Zeyuan Chen [c,d], Haonan Sun [a], Xiaosong Wei [a], Zhuang Ma [a], Jie Li [a], Yayun Bai [a], Zhongming Wu [b,**], Xinge Zhang [a,*]

[a] Key Laboratory of Functional Polymer Materials of Ministry of Education, Institute of Polymer Chemistry, College of Chemistry, Nankai University, Tianjin, 300071, China
[b] NHC Key Laboratory of Hormones and Development, Tianjin Key Laboratory of Metabolic Diseases, Chu Hsien-I Memorial Hospital & Tianjin Institute of Endocrinology, Tianjin Medical University, Tianjin, 300134, China
[c] Tianjin Stomatological Hospital, Tianjin, 300041, China
[d] Hospital of Stomatology, Nankai University, Tianjin, 300071, China

ARTICLE INFO

Keywords:
Bioresponsive materials
Oral biofilm
"Stealthy" corona
Self-modulating
Targeted drug delivery

ABSTRACT

The efficacious delivery of antimicrobial drugs to intractable oral biofilms remains a challenge due to inadequate biofilm penetration and lack of pathogen targeting. Herein, we have developed a microenvironment-activated poly(ethylene glycol) (PEG)-sheddable nanoplatform to mediate targeted delivery of drugs into oral biofilms for the efficient prevention of dental caries. The PEGylated nanoplatform with enhanced biofilm penetration is capable of deshielding the PEG layer under slightly acidic conditions in a PEG chain length-dependent manner to re-expose the bacteria-targeting ligands, thereby facilitating targeted codelivery of ciprofloxacin (CIP) and IR780 to the bacteria after accumulation within biofilms. The nanoplatform tends to induce bacterial agglomeration and suffers from degradation in the acidic oral biofilm microenvironment, triggering rapid drug release on demand around bacterial cells. The self-modulating nanoplatform under near-infrared (NIR) irradiation accordingly displays greatly augmented potency in oral biofilm penetration and disruption compared with drugs alone. Topical oral treatment with nanoplatforms involving synergetic pharmacological and photothermal/photodynamic trinary therapy results in robust biofilm dispersion and efficacious suppression of severe tooth decay in rats. This versatile nanoplatform can promote local accumulation and specific drug transport into biofilms and represents a new paradigm for targeted drug delivery for the management of oral biofilm-associated infections.

1. Introduction

The majority of obstinate infectious diseases in humans, including dental caries and periodontal diseases, are deeply associated with robust bacterial biofilms [1–3]. When bacteria colonize the tooth surface, dense colonies become enclosed in an extracellular matrix composed of polymers such as extracellular polysaccharides (EPS), resulting ultimately in the formation of biofilms [4,5]. Simultaneously, dietary sucrose and other ingredients are fermented by cariogenic bacteria to produce lactic acid and switch the surrounding microenvironment acidic (pH 4.5–5.5) [6–8]. Acidic conditions are favorable for further EPS synthesis and continuous proliferation of cariogenic bacteria, ultimately leading to dental caries [9]. EPS is poorly permeable to antibiotics and other antibacterial agents, and these agents are therefore easily removed by saliva; as a result, effective drug concentrations cannot be maintained in the oral cavity for continuous periods [10,11]. These considerations make the prevention and treatment of pathogenic oral biofilm infections quite challenging [12].

Nanomedicine has presented great potential for anti-biofilm drug delivery due to the unusual advantages for biofilm penetration and intramembrane transport of hydrophobic drugs [13]. To date, various types of nanocarriers such as liposomes [14], polymer micelles [15–17],

☆ Dedicated to the 100th anniversary of Chemistry at Nankai University. Peer review under responsibility of KeAi Communications Co., Ltd.
* Corresponding author.
** Corresponding author.
E-mail addresses: wuzhongming@tmu.edu.cn (Z. Wu), zhangxinge@nankai.edu.cn (X. Zhang).
[1] Yunjian Yu and Yufei Zhang contributed equally to this work.

https://doi.org/10.1016/j.bioactmat.2021.10.035
Received 31 July 2021; Received in revised form 21 October 2021; Accepted 21 October 2021
Available online 2 November 2021

and vesicles [18], have been developed for effective drug delivery into oral biofilms. However, the unstable and complex environment in the oral cavity necessitates a higher ability in biofilm penetration for locally applied nanodrugs. Positively charged nanovehicles have recently emerged to target negatively charged tooth matrix or biofilm components for the enrichment of local drugs [19,20]. However, the nonspecific electrostatic interaction prevents the drug carrier from infiltrating the biofilms deeply, resulting in limited efficacy against oral biofilms [21]. Poly(ethylene glycol) (PEG), which has been extensively recognized as a "stealth molecule" to minimize nonspecific protein adsorption, displays less affinity for EPS in the biofilms as well [22,23]. Therefore, PEGylation could be effective in improving the biofilm penetration of nanocarriers [18,24,25]. However, PEG with excellent stealth properties shows a relatively low affinity for bacterial cells, contributing to a contradictory scenario between PEG-reinforced penetration against EPS and targeted bacteria binding. Although attempts have been made to maximize the electrostatic interactions by synchronous modification of PEG and cationic antimicrobial peptides [18] or employment of pH-activated charge conversion [25,26], PEG shells tend to weaken the targeted effect of positive charges on binding to biofilm bacteria. Similarly, the presence of a PEG layer also tended to impair the specific interaction between the bacteria-targeted ligands derived from the nanoparticle surface and the corresponding receptors on the bacterial cell wall. Therefore, how to achieve coordination between PEG and targeted ligands in a single system is a significant topic for exploration.

With the increasing prevalence of bacterial resistance, a single-pattern delivery strategy based on antibiotics will eventually fail to meet the actual requirements of clinical therapy. Hence, alternative strategies that destroy oral biofilms effectively without generation of bacterial resistance are urgently desired [27,28]. Among these new candidates, photothermal and/or photodynamic therapy (PTT/PDT) hold the most prospect in cancers and bacterial infections due to the robust direct ablation it provides and the negligible possibility of inducing resistance [29,30]. To date, little effort has been devoted to the selective codelivery of antibiotics and light-activated agents in a single system that combines chemotherapy and PTT/PDT for oral biofilm-related infection management.

To address the contradiction between "stealthy" molecule-reinforced biofilm penetration and the low affinity for bacteria, we developed a biofilm microenvironment-induced PEG sheddable light-activated nanoplatform (PS-NP@(C + I)) (Scheme 1), formulated from dual block copolymers of polyethylene glycol-*b*-poly(2-acrylamide glucopyranose) (PEG-*b*-PAGA) and poly(3-acrylamide phenylboronic acid)-*b*-poly(2-(5,5-dimethyl-1,3-dioxan-2-yloxy)ethyl acrylate) (PAAPBA-*b*-PDMDEA) with co-encapsulation of CIP and IR780. The detachable PEG shell is hypothesized to reinforce EPS penetration, thus promoting the efficient drug transport to biofilm-infected lesions. After infiltrating the oral biofilms, the dynamic borate linkages embedded in the interlayer of the nanoplatform dissociated under weakly acidic conditions (pH 6.5) to shed the PEG coating [31], thereby re-exposing the boric acid ligands for specific bacteria anchorage [32]. Meanwhile, the coassembly is subjected to dissociation that initiates the rapid drug release due to the transient hydrolysis of DMDEA moieties immersed in the acidic focal microenvironment (pH 4.7) of oral biofilms. Consequently, the released IR780 is activated upon exposure to 808 nm near-infrared (NIR) light, generating local hyperthermia [33] and cytotoxic reactive oxygen species (ROS) that cooperate with CIP to eradicate the oral biofilms. This versatile nanoplatform has embraced the functions of PEG in biofilm

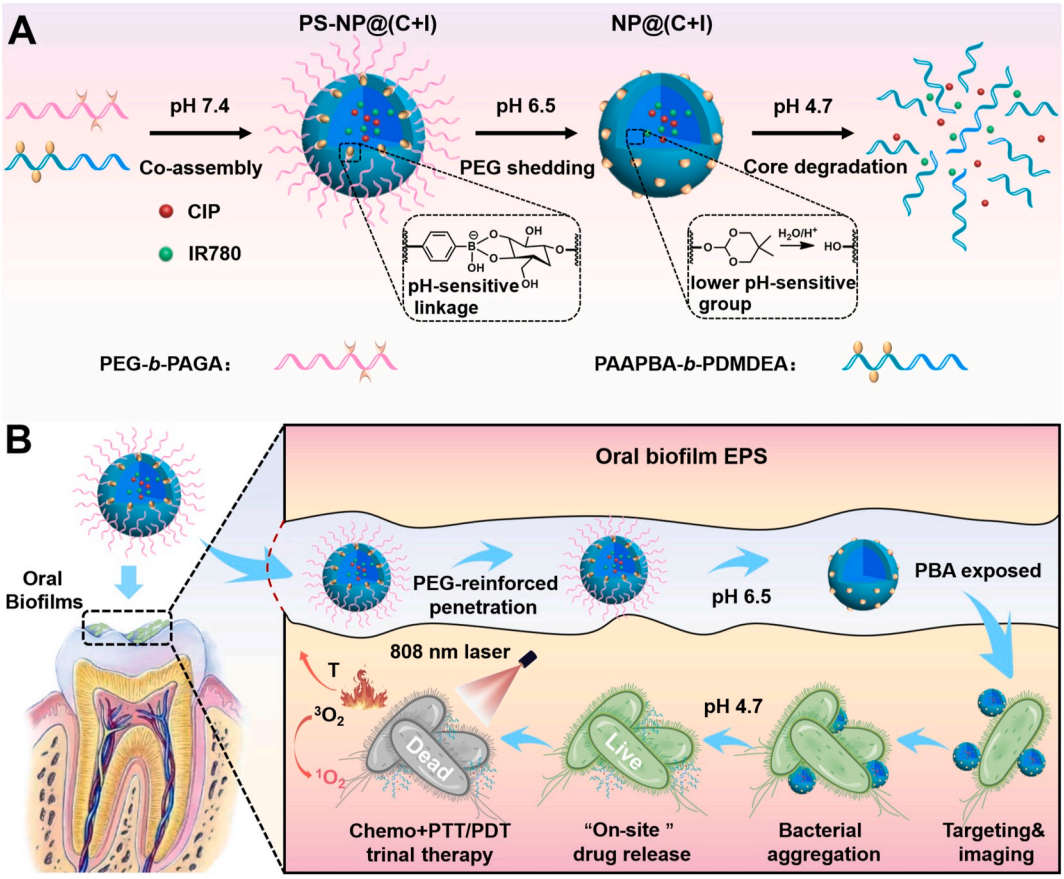

Scheme 1. (A) The formulation of PS-NP@(C + I) to afford a microenvironment-controlled dynamic modulation of nanoplatforms. (B) Schematic illustration of topical codelivery of CIP and IR780 by PS-NP@(C + I) with PEG-reinforced EPS penetration, pH-dependent bacterial targeting and aggregation, and microenvironment-modulated drug release for chemo- and PTT/PDT trinary therapy against *S. mutans* biofilm-induced dental caries.

penetration and bacterial anchorage in a single system. The combination of chemotherapy and phototherapy efficaciously advances the anti-biofilm efficacy and reduces the generation of bacterial resistance, providing a versatile strategy for the clinical treatment of oral biofilm-associated infectious diseases.

2. Experimental section

2.1. Materials

4-Dimethylaminopyridine (DMAP), dicyclohexylcarbodiimide (DCC), monomethoxy-poly(ethylene glycol) (mPEG, M_n = 750, 2000 and 4000 Da) were purchased from Aladdin Bio-Chem Technology Co., Ltd. (Shanghai, China). Azobisisobutyronitrile (AIBN) was provided by Bide Pharmatech Co., Ltd. (Shanghai, China) and used after recrystallization from ethanol. Acryloyl chloride and solvents were distilled before used. Ciprofloxacin, Ciprofloxacin hydrochloride, and 3-(4,5-dime-thylthiazol-2-yl)-2,5-diphenyltetrazolium bromide (MTT) were bought from Heowns Biochemical Technology Co., Ltd. (Tianjin, China). IR780 iodide and FITC labeled Concanavalin A (FITC-Con A) were obtained from Sigma-Aldrich Chemical Co., Ltd. (America). *Streptococcus mutans* (*S. mutans*) CGMCC1.2499, *Lactobacillus acidophilus* (*L.acidopilus*) GDMCC1.321 were provided by China General Microbiological Culture Collection Center (CGMCC) and Guangdong Microbial Culture Preservation Center, respectively, and cultivated according to the standard protocol. The mouse embryonic fibroblast cell line, NIH 3T3, was obtained from American Type Culture Collection (ATCC) and cultured in Dulbecco's modified Eagle's medium (DMEM) supplemented with 10% fetal bovine serum (FBS) and 1% penicillin/streptomycin solution at 37 °C in 5% CO_2/95% air (reagents were all purchased from Gibco (CA, America)).

2.2. Synthesis of Macro-RAFT agent (PEG-CPADB)

4-Cyanopentanoicacid dithiobenzoate (CPADB) was prepared based on previous protocol [34]. To synthesize the macromolecular reversible addition-fragmentation chain transfer agent (Macro-RAFT Agent) PEG-CPADB, mPEG (M_n = 2000 Da, 2.0 g, 1 mmol), CPADB (1.092 g, 4 mmol), and DMAP (0.024 g, 0.2 mmol) were dissolved in 20 mL of freshly distilled dichloromethane. Then DCC (0.618 g, 3 mmol) in 5 mL of dichloromethane was added dropwise via a dropping funnel into the mixture within 0.5 h at 0 °C under continuous nitrogen bubbling. The system was kept stirring for 2 h followed by being heated to room temperature and stirred for another 24 h. After filtration to remove the dicyclohexylurea solid, the resultant red liquid was concentrated and precipitated three times in cold petroleum ether. PEG_{2000}-CPADB was finally received as a pink powder after vacuum drying. PEG_{750}-CPADB and PEG_{4000}-CPADB were obtained likewise following the same method. ^{1}H NMR (400 MHz, $CDCl_3$, 25 °C, Fig. S1) δ (ppm): 1.91 (CH_3, s, 3H), 2.39–2.78 (C–CH_2–CH_2–CO, m, 4H), 3.38 (-O-CH_3, s, 3H), 3.42–3.85 (-(OCH_2CH_2)$_n$O-, m, 4 nH), 4.27 (–COO–CH_2-CH_2-O-, t, 2H), 7.39–7.95 (phenyl in CPADB, m, 5H). GPC: PEG_{750}-CPADB (M_n = 1399, M_w = 1513, PDI = 1.08); PEG_{2000}-CPADB (M_n = 3361, M_w = 3468, PDI = 1.03); PEG_{4000}-CPADB (M_n = 6843, M_w = 7020, PDI = 1.03).

2.3. Synthesis of polyethylene glycol-block-poly(2-acrylamide glucopyranose) (PEG-b-PAGA)

2-Acrylamide glucopyranose (AGA) was synthesized by a similar method with previous literature (Fig. S2) [35]. Using PEG-CPADB as the macro-RAFT agent, the polymerization was performed at [AGA]/[-PEG-CPADB]/[AIBN] = 20:1:0.5 to give copolymer PEG-*b*-PAGA. After bubbling nitrogen into the solution for 0.5 h to remove the air, the reaction was initiated at 70 °C for 24 h with gentle agitation. Afterward, the suspension was cooled in an ice-water bath to quench the polymerization and then dialyzed (MWCO: 3.5 kDa) against water for 3 days with medium change every 4 h for purification. The target block copolymer was afforded ultimately as pale yellow floccule following lyophilization.

2.4. Synthesis of poly (3-Acrylamidophenylboronic acid)-block-poly(2-(5,5-dimethyl-1,3-dioxan-2-yloxy)ethyl acrylate) (PAAPBA-b-PDMDEA)

3-Acrylamidophenylboronic acid (AAPBA), 2-(5,5-dimethyl-1,3-dioxan-2-yloxy)ethyl acrylate (DMDEA) (^{1}H NMR spectrum was shown in Fig. S3), and boron-dipyrromethene dye-conjugated chain transfer agent (BODIPY-RAFT) were synthesized via the method reported previously [36]. The copolymer PAAPBA-*b*-PDMDEA was yielded starting with the RAFT polymerization of PAAPBA at [AAPBA]/[BODIPY-RAFT]/[AIBN] = 20:1:0.25. The system was polymerized at 70 °C for 24 h after 0.5 h of continuous nitrogen bubbling and quenched in an ice-water bath for 10 min. The resulting polymer was precipitated three times in ethyl acetate and given as a light pink block solid after vacuum drying. By distinguishing the feed ratio of AAPBA to BODIPY-RAFT (20:1, 30:1, and 40:1), three distinct homopolymers were obtained abbreviated as $PAAPBA_{20}$, $PAAPBA_{30}$, and $PAAPBA_{40}$, respectively. For synthesis of PAAPBA-*b*-PDMDEA, the RAFT polymerization was carried out at [DMDEA]/[RAFT agent]/[AIBN] = 20:1:0.5 using PAAPBA as macro-RAFT agent. Under standard polymerization protocol the same as that of PAAPBA, the obtained suspension was purified by dialysis against water for 3 days and then freeze-dried to afford PAAPBA-*b*-PDMDEA as a white powder. By altering the macro-RAFT agent, three distinguished block copolymers were obtained and labeled as $PAAPBA_{20}$-*b*-$PDMDEA_{20}$, $PAAPBA_{30}$-*b*-$PDMDEA_{20}$, and $PAAPBA_{40}$-*b*-$PDMDEA_{20}$, respectively.

2.5. Characterization of copolymers

^{1}H NMR spectra of three kinds of PEG-CPADB in $CDCl_3$, PEG-*b*-PAGA in D_2O, and PAAPBA-*b*-PDMDEA in $CDCl_3$/methanol-d_4 (v/v, 12:1) were measured on a Varian Unity-plus 400 NMR spectrometer. Gel permeation chromatography (GPC) measurements were performed at 25 °C on waters 1525 to determine the molecular weight of PEG-CPADB in tetrahydrofuran (THF) and PEG-*b*-PAGA in H_2O. FT-IR spectra of PEG-*b*-PAGA and PAAPBA-*b*-PDMDEA were recorded on a Fourier Transform Infrared Spectrometer (FTS-6000, Bio-Rad Co.).

2.6. Preparation and characterization of PEG-Sheddable copolymeric nanoparticles (PS-NP)

The conventional co-assembly of PEG-*b*-PAGA and $PAAPBA_{40}$-*b*-$PDMDEA_{20}$ was carried out to prepare the PEG-sheddable copolymeric nanoparticles (PS-NP) as the following procedure: 10 mg of PEG-*b*-PAGA was dissolved in 1 mL of DMSO while 10 mg of PAAPBA-*b*-PDMDEA was dissolved in 1 mL of DMSO/H_2O (v/v, 4:1) and the two polymer solutions were mixed homogeneously. Then 14 mL of water was added slowly into the above mixture under robust stirring. The nanoparticle suspension was finally obtained after dialysis against water for 24 h to remove the organic solvent, abbreviating as P_{750}S-NP, P_{2000}S-NP, and P_{4000}S-NP, respectively, in terms of the polymer PEG-*b*-PAGA is PEG_{750}-*b*-PAGA, PEG_{2000}-*b*-PAGA, or PEG_{4000}-*b*-PAGA. The nanoparticles formulated from $PAAPBA_{20}$-*b*-$PDMDEA_{20}$, $PAAPBA_{30}$-*b*-$PDMDEA_{20}$, and $PAAPBA_{40}$-*b*-$PDMDEA_{20}$ were denoted as NP1, NP2, and NP3, respectively. The hydrodynamic diameter (D_H), polydispersity index (PDI), and zeta potential of copolymeric nanoparticles were determined by dynamic light scanning (DLS, Zetasizer Nano ZS90) and the morphology was observed under a transmission electron microscopy (TEM, Tecnai G2 F20).

2.7. PEG shedding behavior of PS-NP

Five milligrams of PS-NP (P_{750}S-NP, P_{2000}S-NP, or P_{4000}S-NP) at a

concentration of 10 mg/mL were placed in a centrifuge tube containing 15 mL of phosphate-buffered saline (PBS) (0.01 M, pH 7.4 or pH 6.5), and the mixture was shaken at a constant speed (200 rpm/min) in a thermostatic oscillator at 37 °C. The liquid in the tube was concentrated (10000 rpm, 30 min) at predetermined times (1, 2, 4, 6, 12, and 24 h), and 0.8 mL of the supernatant was withdrawn and diluted with an equal volume of fresh buffer. To determine PEG shedding from PS-NPs, the PEG content of the sample was measured using an iodide staining method as described in the previous literature [37,38]. Briefly, standards (1–10 μg/mL) were diluted in 1 mL of PBS (0.01 M, pH 7.4). To this, 50 μL of a mixed solution containing iodine (5 g/L) and potassium iodide (10 g/L) was then added. The absorbance of the sample at 500 nm was measured, and standard curves for each of the three types of PEG chains were obtained by linear fitting. Unknown samples obtained at different times were measured using the same method, and the concentration of released PEG was determined according to the corresponding standard curve.

2.8. Bacterial aggregation and imaging

The bacterial aggregation performance of PS-NP at different pH values (pH 7.4 or pH 6.5) was evaluated by confocal laser scanning microscopy (CLSM) first. Briefly, *S. mutans* was cultivated overnight in brain heart infusion broth (BHI) at 37 °C. After being concentrated (5000 rpm, 5 min) and redispersed in PBS, the bacteria were then diluted to allow the optical density at 600 nm (OD_{600}) to close to 2.0. The working bacterial suspension was statically incubated with isopyknic nanoparticle solution with various pH values (pH 7.4 or pH 6.5) at 37 °C for 2 h. Then the aggregated bacterial samples were redispersed in 70% glycerin thoroughly and observed on CLSM (TCS SP8).

The solution-turbidity method was further utilized to investigate the time-dependent aggregation behavior of *S. mutans* by PS-NP. Similarly, the prepared bacterial suspension was co-cultured in equal volume with the nanoparticle solution in pH 7.4 or pH 6.5 at 37 °C. The bacterial supernatant was withdrawn every 20 min to determine the floating bacteria content by measuring OD_{600} on a UV–vis spectrophotometer (UV-2550). The bacteria treated with PBS buffer (0.01 M, pH 7.4) were set as the control group. Each sample was performed in triplicate.

To analyze the imaging potential of fluorescent PS-NP for bacterial cell wall, the fresh *S. mutans* was redispersed in PBS buffer (0.01 M, pH 7.4) and modulated the concentration to give $OD_{600} = 1.0$. Then the working bacterial suspension was incubated in equal volume with the PS-NP solution (P_{750}S-NP, P_{2000}S-NP, or P_{4000}S-NP) at 37 °C for 2 h. After being concentrated (5000 rpm, 5 min) and washed three times with PBS buffer to eliminate the non-aggregated bacterial cells and free nanoparticles, the bacteria were stained by DAPI and resuspended in 70% glycerin followed by observation on CLSM.

2.9. Preparation and characterization of CIP- and IR780-Loaded PEG-sheddable nanoparticles (PS-NP@(C + I))

The CIP- and IR780-loaded PS-NP (PS-NP@(C + I)) was prepared under a similar procedure to PS-NP with the additional participation of CIP and IR780. By changing the feed weight ratio of CIP or IR780 to copolymers, various drug-loaded nanoparticles were obtained for the determination of loading capacity and optimization of the dosage ratio of the two drugs. To determine the encapsulation efficiency (EE) and loading capacity (LC) of PS-NP toward CIP and IR780, the freshly prepared nanoparticle solution before purification was concentrated (12000 rpm, 50 min) and the content of CIP or IR780 in the supernatant was measured using the UV method at 278 or 790 nm with the help of calibration curves (Fig. S5), respectively. EE and LC were finally calculated in terms of the following formula:

$$\mathrm{EE} = \frac{\text{Weight of encapsulated drug}}{\text{Weight of total drug}} \times 100$$

$$\mathrm{LC} = \frac{\text{Weight of encapsulated drug}}{\text{Weight of drug loaded nanoparticles}} \times 100$$

2.10. In vitro CIP release

The *in vitro* CIP release profiles of PS-NP@(C + I) were studied at different pH values (pH 7.4 pH 6.5, and pH 4.7). P_{2000}S-NP@(C + I) solutions (5 mL) were transferred into a dialysis tube (MWCO: 3.5 kDa) and then immersed into a centrifuge tube (50 mL) containing 15 mL of buffer solution and shook at 37 °C at a constant speed of 200 rpm/min. At scheduled time points (0.17, 0.5, 1, 2, 4, 6, 8, 12, 24, and 48 h), 0.4 mL of external buffer solution was withdrawn and supplemented with isopyknic fresh buffer. After dilution with HCl solution (0.4 mL, 0.1 M), the samples were examined on a UV–vis spectrophotometer at 278 nm to determine the content of released CIP.

2.11. Determination of NIR-Activated ROS generation and temperature raising of PS-NP@(C + I)

The ROS generation of IR780 entrapped in P_{2000}S-NP@(C + I) upon irradiation with 808 nm laser was determined by using DCFH-DA as the ROS trapping agent [39]. Briefly, the nanoparticle suspension in PBS with various concentrations of IR780 (30, 60, and 120 μg/mL) and free IR780 (120 μg/mL) were severally mixed the DCFH-DA PBS buffer (0.01 M, pH 7.4) solution. Setting pure water as a negative group. Subsequently, the suspensions were all exposed to the 808 nm laser (1.5 W/cm^2) for different periods (1, 2, 3, 4, and 5 min). The fluorescence intensity of DCFH, an oxidation product of DCFH-DA, was analyzed and quantified by the fluorescence spectrophotometer (RF-5301PC) and the small animal imaging system (IVIS Lumina III), respectively, the excitation wavelength was 488 nm. Meanwhile, to demonstrate the temperature increase of solution under 808 nm laser (1.5 W/cm^2) irradiation, the pseudo-color images of nanoparticle suspensions were taken every 0.5 min by a thermal infrared imager.

2.12. MTT assay

The cell viability of copolymeric nanoparticles was evaluated by MTT assay. NIH 3T3 cells were seeded in 96-well plates at a density of 1×10^4 cells/well and allowed to adhere overnight at 37 °C with 5% CO_2/95% air. Afterward, the cells were exposed to the copolymeric nanoparticles for 24 h using the double dilution method by DMEM, starting at a concentration of 500 μg/mL. The cells that do not receive any treatment were used as a control group. Then, 10 μL of MTT solution (5%) in PBS was added into each well and the mixtures were further incubated for another 4 h. The media were removed DMSO (150 μL) was added to thoroughly dissolve the formazan crystals. The optical density at 490 nm was read on Microplate Reader (Molecular Devices, USA). The relative cell viability was calculated as a percentage compared with that of the control group.

$$\text{The relative cell viability} = \frac{A_t - A_0}{A_c - A_0} \times 100\%$$

Where A_t is the absorbance of cells treated by nanoparticles, A_c is the absorbance of cells in the control group, and A_0 is the absorbance of the plate.

2.13. In vitro antibacterial experiments

2.13.1. Bacterial growth inhibition assays

S. mutans in the fast-growing period at a concentration of 2×10^7 CFU/mL were subjected to incubation with an array of equivalent double-diluted antibacterial materials in PBS at 37 °C. The bacteria treated with PBS (0.01 M, pH 7.4) were set as a negative control group. After 2 h of incubation, the bacteria in light irradiation groups were

exposed to 808 nm laser (1.5 W/cm^2) for 5 min, and incubated for another 8 h. Then the bacterial growth inhibition was evaluated by measuring the OD_{600} value of the treated bacterial sample on a UV–vis spectrophotometer.

2.13.2. BHI plate counting

A 1 mL aliquot of *S. mutans* suspension (2×10^8 CFU/mL) in PBS buffer (0.01 M, pH 7.4) was co-cultured with 1 mL of various antibacterial agents (free CIP, P_{2000}S-NP@CIP, P_{2000}S-NP@IR780, and P_{2000}S-NP@(C + I)) at 37 °C for 2 h. The bacteria treated with PBS (0.01 M, pH 7.4) were served as a negative control group. After being irradiated with an 808 nm laser (1.5 W/cm^2) for 5 min, the bacteria were then diluted to grow on the BHI agar plate overnight at 37 °C. The number of colony-forming units (CFUs) of each group was counted and photographed for comparing antibacterial efficacy.

2.13.3. Live/dead fluorescent assays

The fresh bacterial cells were diluted with PBS buffer (0.01 M, pH 7.4) to give a concentration of 2×10^8 CFU/mL and then incubated with free CIP, P_{2000}S-NP@CIP, P_{2000}S-NP@IR780, and P_{2000}S-NP@(C + I), respectively. The bacteria treated with PBS (0.01 M, pH 7.4) were served as the negative control group. After 2 h of incubation at 37 °C, the bacteria in light irradiation groups were exposed to an 808 nm laser (1.5 W/cm^2) for 5 min. Subsequently, all samples were concentrated (5000 rpm, 5 min) to remove the free materials, stained with acridine orange (AO) and ethidium bromide (EB) at 4 °C in dark, and then washed three times with sterile PBS buffer. Finally, the samples were examined by CLSM.

2.13.4. Observation of bacterial morphology

To observe the morphology of the bacteria after incubation with nanoparticles and exposure to an 808-nm laser (1.5 W/cm^2), the treated samples were concentrated (5000 rpm, 5 min) to eliminate redundant materials and resuspended in sterile PBS. A moderately dense bacterial suspension was applied to a silicon pellet and fixed with glutaraldehyde solution (2.5%, v/v) for 4 h. After several washes with sterile PBS, the bacteria were dehydrated in a series of ethanol aqueous solutions (30%, 50%, 70%, 90%, 95%, and 100%, v/v) and dried overnight at room temperature. Ultimately, the samples were observed on a scanning electron microscope (SEM, JSM-7500F).

2.14. Biofilm penetration

To investigate the penetration of P_{2000}S-NP@NIL into *S. mutans* biofilms, *S.mutans* was cultured overnight in BHI medium at 37 °C and diluted with medium containing 0.5% sucrose to allow the OD_{600} value of bacteria to close to 0.025. Then the prepared bacterial suspension was seeded in a 6-well plate with sterile coverslips (18 × 18 mm) vertically placed and cultured statically at 37 °C for 48 h. When the mature biofilms were formed on the coverslips, the media were removed and the biofilms were washed three times with sterile PBS buffer to separate the planktonic bacteria. The biofilms were then exposed to P_{2000}S-NP@NIL in suspension (500 μg/mL) at pH 7.4 or pH 6.5 for 4 h, washed with PBS to remove the free P_{2000}S-NP@NIL, fixed with paraformaldehyde (4%, w/v), stained with FITC-labeled concanavalin A (FITC-ConA) and imaged using CLSM.

2.15. Biofilm dispersion assays

The freshly prepared bacterial suspension (OD_{600} = 0.025) was seeded in a 96-well plate and cultured statically at 37 °C for 24 h. When the mature biofilms were formed on the walls of wells at the interface between the media and the air, the media were removed and the biofilms were washed three times with sterile PBS buffer to separate the planktonic bacteria. Thereafter, a pool of double-diluted free CIP, P_{2000}S-NP@CIP, P_{2000}S-NP@IR780, or P_{2000}S-NP@(C + I) in PBS (150 μL) were added into the wells to incubate with the biofilms, respectively, setting the biofilms treated with PBS as the negative control group. Concentration of polymers: 31.25, 62.5, 125, 250, 500 μg/mL; Concentration of loaded IR780: 3.75, 7.5, 15, 30, 60 μg/mL; Concentration of loaded CIP: 3.45, 6.9, 13.8, 27.5, 55 μg/mL, and the concentration of free CIP is the same as that of loaded CIP in nanoparticles. After 4 h of co-culture at 37 °C, the biofilms of light irradiation groups were exposed to 808 nm laser (1.5 W/cm^2) for 5 min followed by a triple wash with sterile PBS buffer to remove the redundant non-adherents. Then the biofilm was fixed with methanol for 15 min and dyed with 0.5% crystal violet PBS solution for 15 min. The biofilms were washed adequately with sterile PBS, and crystal violet was dissolved in 33% acetic acid (v/v) for 10 min with gentle shaking. The absorbance of the solution at 590 nm was read on a microplate reader (384 Plus) to quantify the biofilm content of the sample. Each sample was analyzed in quintuplicate. The antibiofilm efficacy of the light therapeutic agent as a function of irradiation time was investigated by following the above steps.

To visually observe the biofilm obliteration by the applied materials, the matured biofilms on the coverslips were treated with free CIP, P_{2000}S-NP@CIP, P_{2000}S-NP@IR780, or P_{2000}S-NP@(C + I), respectively, at a consolidated concentration of 110 μg/mL for CIP and 120 μg/mL for IR780. The biofilms treated with PBS were set as negative control groups. After 5 min of irradiation with 808 nm laser (1.5 W/cm^2), the biofilms were fixed by glutaraldehyde solution (2.5%, v/v) for 4 h and stained with FITC-ConA for 15 min at 4 °C in dark. Finally, the prepared biofilm samples were observed by CLSM-3D.

2.16. Ex vivo antibiofilm performance on natural teeth from human

To further explore the antibiofilm performance of P_{2000}S-NP@(C + I) plus NIR irradiation, an *ex vivo* biofilm model was used to examine whether the topical treatments can disrupt cariogenic biofilm development. The excised human teeth received from volunteers in Tianjin Stomatological Hospital were processed by a professional dentist to remove the root and retain the crown with 30% H_2O_2 and washed five times with sterile PBS (0.01 M, pH 7.4). The isolated teeth were placed in a 24-well plate and immersed with the bacterial suspension (*S. mutans* or *L. acidopilus*) in BHI or MRS medium containing 0.5% sucrose (OD_{600} = 0.025). The teeth were then coincubated with the bacterial suspension at 37 °C for 48 h. Afterward, the media in the 24-well plates were removed, and the biofilms were washed three times with sterile PBS to isolate the planktonic bacteria. The teeth were treated with a pool of P_{2000}S-NP@CIP, P_{2000}S-NP@IR780, or P_{2000}S-NP@(C + I) solutions, setting the isolated teeth treated with PBS as the negative control group. After 2 h of co-culture at 37 °C, the teeth in light irradiation groups were exposed to 808 nm laser (1.5 W/cm^2) for 5 min followed by a triple wash with sterile PBS to remove the redundant non-adherents. Then the teeth were fixed with methanol and dyed with 0.5% crystal violet solution. The biofilms were washed adequately with sterile PBS, and crystal violet was dissolved in 33% acetic acid (v/v) with gentle shaking. The absorbance of the solution at 590 nm was read on a microplate reader (384 Plus) to quantify the biofilm contents.

2.17. In vivo study

Animal experiments were reviewed and approved by the Animal Ethics Committee of the Institute of Radiation Medicine Chinese Academy of Medical Sciences (SYXK(J) 2019-0002). All animals were maintained following the guidelines outlined in the Guide for the Care and Use of Laboratory Animals. Briefly, 19-day-old female Sprague-Dawley rat pups were purchased from Beijing HFK Bioscience Co., Ltd. and screened for infection with *S. mutans* by plating oral swabs on Mitis Salivarius Agar plus Bacitracin (MSB). Rats that were already infected with *S. mutans* were culled. The remaining animals were infected by mouth with *S. mutans* (CGMCC1.2499) in the exponential growth phase, which corresponds to bacteria that are actively growing

in the oral cavity. On the 21st day, colonization of the oral cavity by *S. mutans* was confirmed by buccal swab. The formation of biofilm on the surface of the tooth was indicated by visualized crystal violet staining. The animals had free access to the National Institute of Health cariogenic diet 2000 and water containing 5% sucrose. We applied a treatment regimen consisting of topical application of P_{2000}S-NP@(C + I) for 5 min by using a custom-made applicator, a spacing interval of 15 min, and 5 min of irradiation with an 808 nm NIR laser (1.5 W/cm^2). The irradiation began to perform after the mice were immobilized and anesthetized by isoflurane. The infected pups were randomly divided into five groups (n = 6 per group) that received the following treatments: (1) PBS plus NIR laser; (2) free CIP; (3) P_{2000}S-NP@CIP; (4) P_{2000}S-NP@IR780 plus NIR laser; and (5) P_{2000}S-NP@(C + I) plus NIR laser. The applied concentration of CIP was 27.5 μg/mL, and that of IR780 was 30 μg/mL, these values were maintained for free and loaded form. The animals were treated once every two days for three weeks and weighed weekly. To validate whether the obtained drug delivery system can penetrate biofilms on the surface of the tooth, the teeth of rat pups after being infected with *S. mutans* were isolated and placed in a 12-well plate. The prepared P_{2000}S-NP@NIL was then added to the plate and cultured with the teeth at 37 °C for 15 min. Afterward, the teeth were washed several times with sterile PBS, stained with FITC-ConA at 4 °C in dark for 30 min, and finally examined by CLSM-3D. Simultaneously, the isolated teeth were dyed with 0.5% crystal violet solution for 15 min and photographed using a video camera.

At the end of the experimental period, the animals were sacrificed, and their jaws were surgically removed and aseptically dissected, followed by sonication to recover the total oral microbiota [40]. All jaws were defleshed, and the teeth were prepared for caries scoring by two oral pathologists (Dr. Wang and Dr. Chen, Tianjin Stomatological Hospital) according to Larson's modification of Keyes' system [15,41,42]. The alveolar caries score was determined by a calibrated examiner who was unfamiliar with the study and used coded samples. Furthermore, the gingival and palatal tissues were collected and processed for hematoxylin and eosin (H&E) staining for histopathological analysis by the oral pathologists.

3. Results

3.1. Preparation and characterization of PS-NP

The programmable nanoplatform serving as the antibiofilm drug carrier was fabricated by coassembly of PEG-*b*-PAGA and PAAPBA-*b*-PDMDEA copolymers via hydrophilic-hydrophobic and phenylboronic acid (PBA)-polysaccharide interactions. It is generally accepted that biofilm penetration greatly influences the therapeutic efficacy of drug delivery systems [43]. A nanoplatform with a low affinity for exogenous matrices and biological particulates has been shown to exhibit superior biofilm penetration and diffusion owing to the reduced blockade of EPS in biofilms [18,25,26]. Such a strategy is ordinarily achieved by surface functionalization or remodeling to produce a nonadherent shell of nanoparticles. Generally, PBA and its derivatives have been shown to possess a robust affinity for the cell walls of a broad spectrum of bacteria, and this facilitates active targeting via specific PBA-diol interactions [44,45]. However, the antifouling shell hinders the attachment of nanoparticles to pathogens and even the specific binding of PBA ligands to the targeted bacterial cells in biofilms. To address this contradiction, we developed a simple strategy for the fabrication of a microenvironment-controlled shell-sheddable nanoplatform that utilizes a PEG corona to facilitate biofilm EPS penetration and thereby efficiently enhance drug accumulation; this nanoplatform sheds the "stealthy" layer within the biofilm, re-exposing the bacteria-targeting ligands for bacterial aggregation and imaging and releasing the loaded drugs "on-site" in response to the acidic oral biofilm macroenvironment. Shell detachment is achieved by the introduction of acid-labile boronate ester linkages. In our design, dual copolymers of PEG-*b*-PAGA and PAAPBA-*b*-PDMDEA were coassembled into PEG-sheddable nanoparticles (abbreviated PS-NPs) to create a nanoplatform with a "stealthy" PEG shell, a cross-linked borate layer and an acid-converted PDMDEA core (synthetic characterization of polymers was presented in supporting information, Scheme S1, Figs. S1–4 and Table S1). To investigate the effect of PEG content on the shedding behavior, three nanoparticles with different PEG chain lengths (M_n = 750, 2000, and 4000 Da) were prepared and designated P_{750}S-NP, P_{2000}S-NP, and P_{4000}S-NP, respectively. The PEG-free nanoparticles (NP1, NP2, and NP3) formulated from the PAAPBA-*b*-PDMDEA copolymers with varying AAPBA content were found by dynamic light scattering (DLS) to exhibit sizes ranging from 70 to 90 nm (Table S2). In contrast, the sizes of PS-NPs increased to different degrees within an overall range of 117–170 nm and showed a moderate polydispersity index (PDI) (Table S2). The change in PDI from above 0.2 for NP to below 0.2 for PS-NP implies a significant role of the PEG shell in particle stabilization. The nanoparticles were all negatively charged whether in the presence of PEG shell or not (Table S2). P_{4000}S-NPs at pH 7.4 were observed by TEM to be spherical and approximately 150 nm in diameter with good dispersity (Fig. 1A). At pH 6.5, P_{4000}S-NP, which displayed a fuzzy halo-featured edge, showed a smaller size (below 100 nm) equivalent to that of NP (Fig. 1B), demonstrating the detachment of the PEG shell from P_{4000}S-NP following the dissociation of the cross-linked boronate ester bonds under slightly acidic conditions. At a lower pH of 4.7, the ortho-ester cores of P_{4000}S-NP underwent hydrolysis, giving rise to a blurred, irregular and destroyed shape under TEM (Fig. 1C) [46]. The observed pH-dependent change in the size of the particles was consistent with the results determined by DLS (Fig. 1D). The UV–vis absorption and fluorescence emission spectra of BODIPY dye-labeled PS-NPs were examined and found to present a well-defined bandwidth with maximal absorption at 505 nm and maximal emission at 517 nm (Fig. 1E).

3.2. PEG shedding behavior of PS-NP

To demonstrate the PEG shedding behavior of PS-NPs, P_{4000}S-NPs were treated with pH 7.4 or pH 6.5 buffer and concentrated to harvest the supernatants. The ^{1}H NMR spectra showed that there was more PEG in the supernatant of nanoparticles treated in the medium at pH 6.5 than in the supernatant of nanoparticles treated in the medium at pH 7.4 (Fig. 1F), providing proof of borate dissociation-mediated PEG shell detachment from P_{4000}S-NP under weakly acidic conditions. To further explore the effect of PEG chain length on shell shedding behavior, the three types of nanoparticles (P_{750}S-NP, P_{2000}S-NP, and P_{4000}S-NP) were similarly treated with pH 7.4 or pH 6.5 buffer, and PEG release from the nanoparticles was tracked throughout 24 h using an iodine staining method. As seen in Fig. 1G–I, about 10% of PEG was shed from the three types of nanoparticles after 24 h of incubation at pH 7.4. This phenomenon could be attributed to the weak physical absorption of partial PEG chain on the surface of nanoparticles during self-assembly, which would preferentially be detached under shaking conditions. In comparison, P_{750}S-NP shed approximately 43% of the PEG layer within 24 h, while P_{2000}S-NP and P_{4000}S-NP reached cumulative PEG shedding of approximately 51% and 31%, respectively, when incubated at pH 6.5, further indicating a pH-dependent PEG shell detachment phenomenon of PS-NPs. The data suggest that among the three types of nanoparticles, P_{2000}S-NPs display the most rapid PEG shedding behavior in response to slightly acidic conditions, and this may be an important factor in the final choice of nanoparticles for further investigation.

3.3. pH-dependent bacterial aggregation and imaging performance of PS-NPs

As previously mentioned, PBA groups and their derivatives can specifically bind to both gram-negative and gram-positive bacteria [47]. To evaluate the bacterial binding and aggregation performance of the PBA-anchored nanoparticles toward *S. mutans* (an oral pathogen that

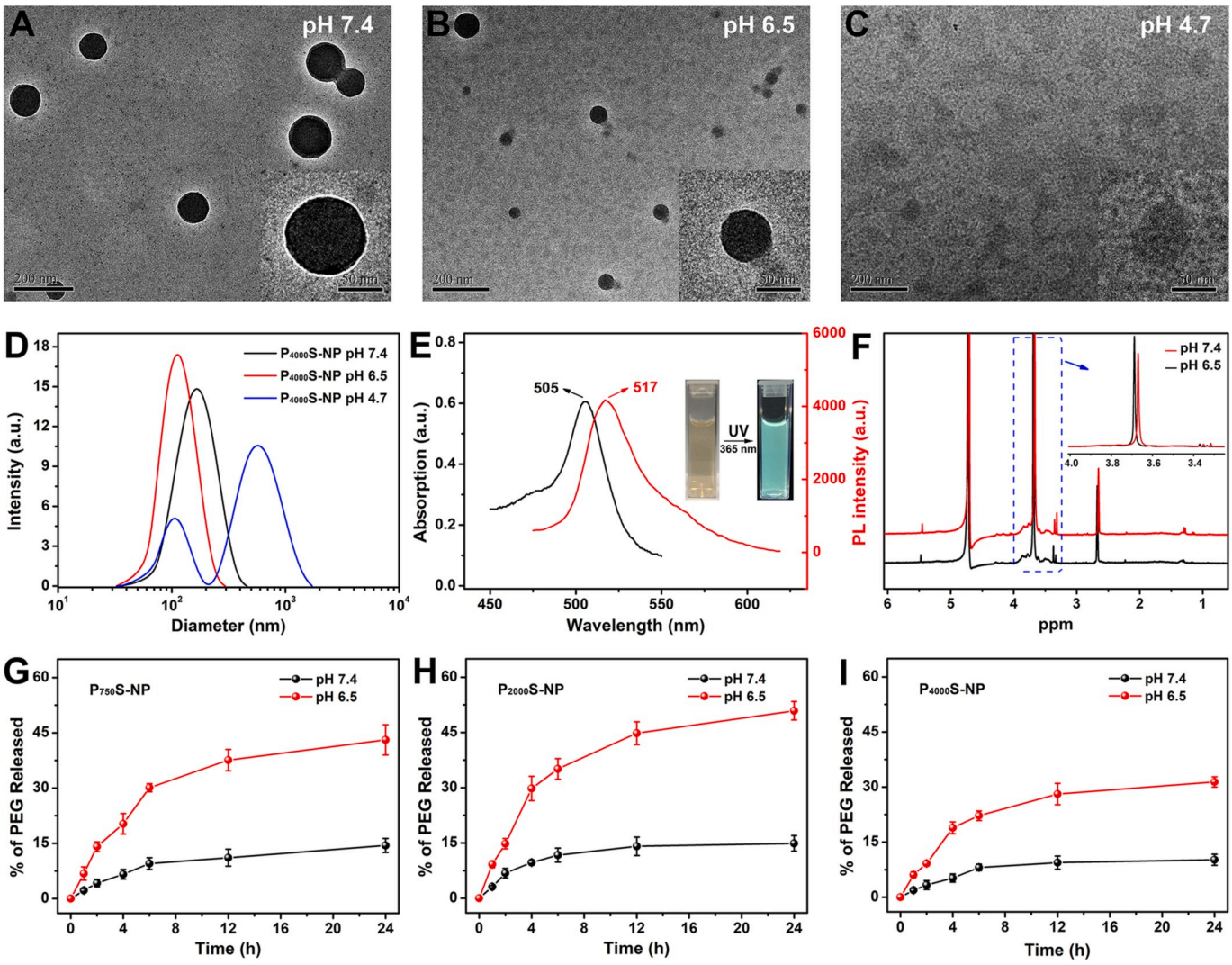

Fig. 1. TEM images of P_{4000}S-NP at pH 7.4 (A), pH 6.5 (B) and pH 4.7 (C); (D) size distribution of P_{4000}S-NP at different pH values determined by DLS; (E) UV–vis absorption (black curve) and fluorescence emission (red curve) spectra of P_{4000}S-NP (insets: photographs of P_{4000}S-NP under white light or 365 nm ultraviolet light); (F) ^{1}H NMR of P_{4000}S-NP under various pH conditions in D_2O; PEG shedding from (G) P_{750}S-NP, (H) P_{2000}S-NP and (I) P_{4000}S-NP at various pH values, the results were reported as mean ± s.d. ($n = 3$).

can induce dental decay) at different pH values, the bacteria were incubated with PS-NPs (P_{750}S-NP, P_{2000}S-NP, and P_{4000}S-NP) in pH 7.4 or 6.5 medium for 2 h at 37 °C and observed under confocal laser scanning microscopy (CLSM). Bacteria treated with PBS at pH 7.4 or 6.5 were set as the control (Fig. S6). As shown in Fig. 2A, *S. mutans* cells were found to exhibit strong green fluorescence stemming from the BODIPY dye and to aggregate into clusters whose size was a function of the AAPBA content after treatment with NP (NP1, NP2, and NP3) at pH 7.4. However, bacterial cells treated with PS-NP at pH 7.4 were aggregated into much smaller clusters compared to the NP-treated ones, suggesting that the presence of a "stealthy" PEG layer impedes the multivalent interaction between PS-NP and the cell walls of *S. mutans*. In contrast, it was observed that all PS-NPs caused the bacterial cells to form larger fluorescent clusters at pH 6.5 than at pH 7.4, thereby achieving a bacterial aggregation profile comparable to that produced by exposure to NP3. This phenomenon implies that the bacterial binding capacity of PS-NP recovered upon the dissociation of borate ester linkages and the detachment of the PEG shell under slightly acidic conditions. Notably, the bacterial clusters formed in the presence of P_{2000}S-NP at pH 6.5 were larger than the clusters formed in the presence of the other two types of nanoparticles, indicating that P_{2000}S-NP undergoes the most efficient PEG shedding and exerts the function of PBA to the greatest extent, consistent with the results of our PEG release assays.

The solution turbidity method was employed to further determine the bacterial agglomeration performance of PS-NPs at different pH values, taking P_{2000}S-NPs as an example. *S. mutans* cells were incubated with P_{2000}S-NP at pH 7.4 or pH 6.5, and PBS was used as a control. The OD_{600} values of the bacterial supernatants were recorded during 2 h of treatment to indicate the sedimentation of bacteria-nanoparticle aggregates. As shown in Fig. 2B and C, bacteria treated with PBS at pH 7.4 or 6.5 for 2 h showed a natural sedimentation rate of 20%–30% with a slow rate. By contrast, the OD_{600} of NP3-treated bacteria declined rapidly over time, while about 75% of bacteria were aggregated by NP3 and sank from supernatant into bottom within 2 h whether at pH 7.4 or 6.5, indicating the intrinsic bacterial aggregation ability of PBA-based nanoparticles. Notably, only 60% of bacteria sank to the bottom after treatment with P_{2000}S-NP for 2 h at pH 7.4 in the presence of NP3 with PEG shell, which impaired the interaction between PBA groups and bacteria. At pH 6.5, however, exposure to P_{2000}S-NP induced a bacteria settlement rate of 70% within 20 min and 79% within 2 h due to the detachment of PEG shell from the nanoparticles at pH 6.5, achieving a bacterial sedimentation effect similar to that obtained with NP3. The results further demonstrate the pH-dependent bacterial aggregation behavior of PS-NPs, whose PBA groups were highly exposed and bound

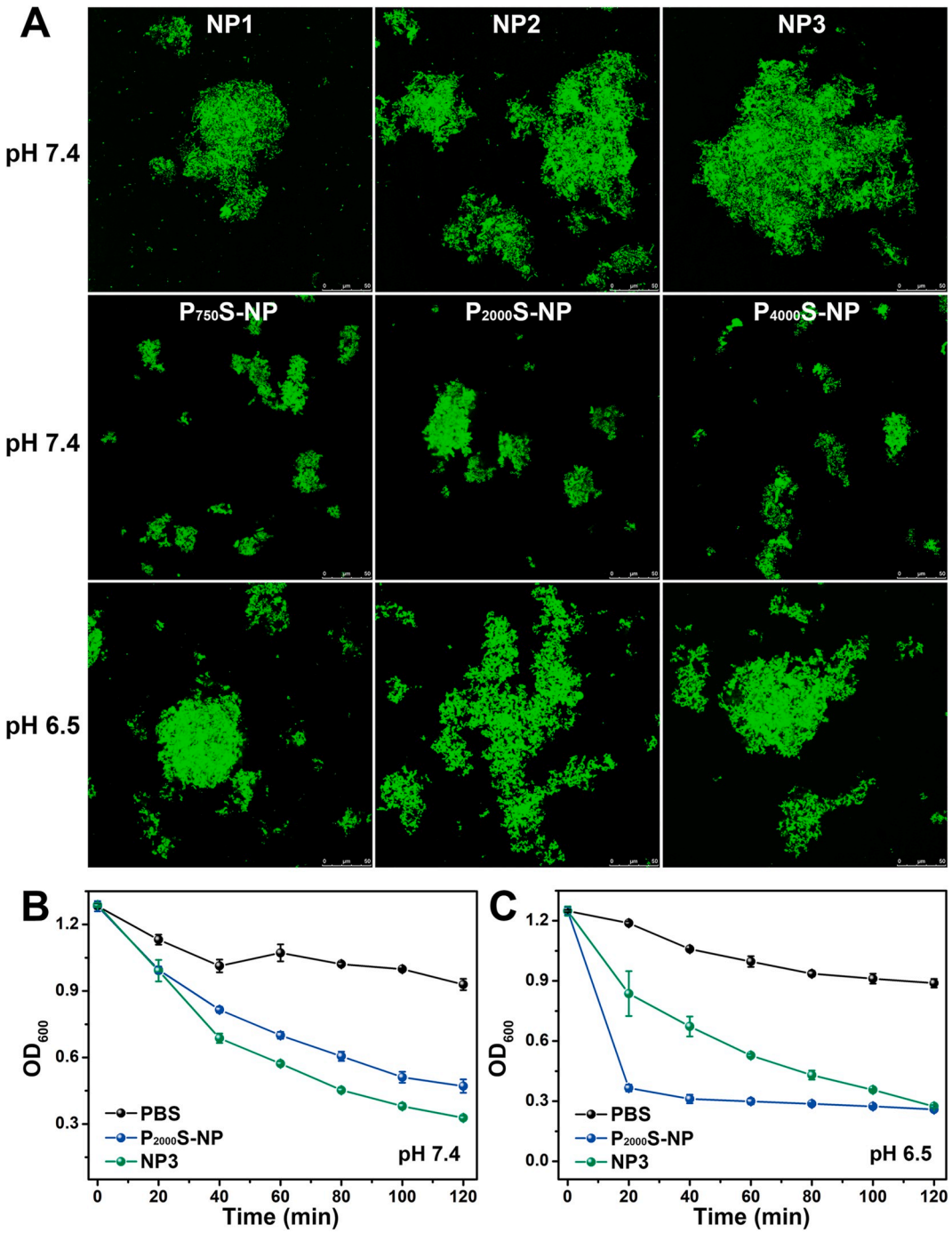

Fig. 2. (A) Aggregation of *S. mutans* observed by CLSM after incubation with P_{750}S-NP, P_{2000}S-NP, or P_{4000}S-NP at 37 °C for 2 h at pH 7.4 or pH 6.5. Green fluorescence: BODIPY moieties in the nanoparticles. (B, C) OD_{600} value of *S. mutans* as a function of incubation time with PBS, P_{2000}S-NP, and NP3 at pH 7.4 (B) or pH 6.5 (C). Each experiment was performed in triplicate, and the results were presented as mean ± s.d. ($n = 3$). The concentration of all nanoparticles was 500 μg/mL.

to bacteria under the mechanism of PEG shell detachment in a weakly acidic environment.

As shown by the CLSM observation, the bacteria could be imaged using BODIPY-derived fluorescent nanoparticles. We further investigated the differences in bacterial imaging observed after exposure of the bacteria to the three types of PS-NPs before and after the detachment of PEG. As shown in Fig. 3A and B, whole bacterial cells in the clusters were labeled with green fluorescence from BODIPY molecules after treatment with NP3, implying that the PEG-free nanoparticles could penetrate the bacterial cell wall and enter the cell interior. CLSM-3D images presenting the merge of green fluorescent signals from NP with the blue fluorescence signals from bacteria further demonstrated that the status of PEG-free nanoparticles inside the bacterial cells (Fig. S7). However, bacteria treated with any of the three types of PS-NPs showed BODIPY signals only on their outer surfaces, indicating that the PEG-decorated nanoparticles could stain the bacterial cell wall. The difference in the appearance of the bacteria might be attributed to the presence of the PEG shell, which prevents the functional targeting ligand of PBA from binding efficiently to the bacterial cell wall. In addition, there were differences in the cell wall staining profiles observed after treatment with the three types of PS-NPs; P_{750}S-NP stained the cell wall most completely, followed by P_{2000}S-NP and P_{4000}S-NP, demonstrating that

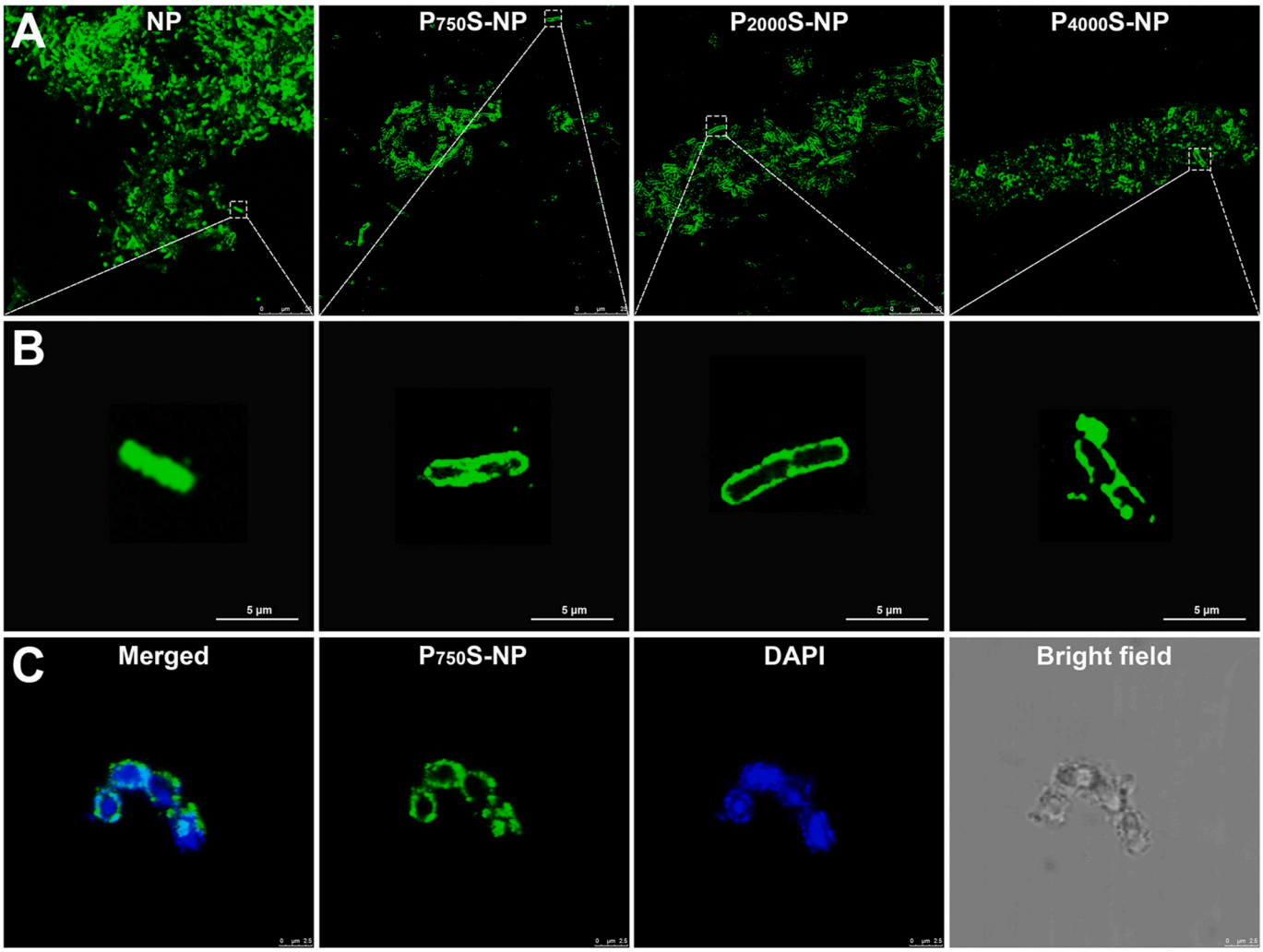

Fig. 3. CLSM images of *S. mutans* (A) and locally enlarged bacteria (B) after treatment with NP, P_{750}S-NP, P_{2000}S-NP, or P_{4000}S-NP at 37 °C for 2 h at pH 7.4; (C) CLSM images of P_{750}S-NP-treated *S. mutans* stained with DAPI.

the impediment caused by the PEG shell was chain length-dependent: the longer the PEG chain was, the greater was the impediment. We further used DAPI to stain the bacteria, especially the interior of the bacteria (Fig. 3C). The green P_{750}S-NP fluorescence was evenly distributed on the bacterial cell wall and partially overlapped the blue DAPI signal, further proof that PS-NP images the bacterial cell wall. The overlap of the fluorescent signal provides evidence that interactions occur between the PBA groups in the nanoparticles and the DNA components of the bacterial cell wall [48]. Based on its overall behavior concerning PEG shedding and bacterial aggregation, we chose to use P_{2000}S-NP in further investigations.

3.4. Preparation and characterization of PS-NP@(C + I)

To obtain a NIR-activated anti-biofilm agent with multiple pipelines in parallel that responds to the oral biofilm microenvironment, the broad-spectrum antibiotic CIP and the near-infrared molecule IR780 were co-encapsulated into P_{2000}S-NP, yielding nanoparticles that we designated P_{2000}S-NP@(C + I), as portrayed in Fig. 4A. The optimal feed ratios of CIP and IR780 in the copolymers were determined to be 0.24 and 0.24, respectively; this was done by separately varying the feed ratios of the drugs and comparing the resulting physicochemical parameters of the nanoparticles (Fig. 4B and C, Tables S3 and S4). The CIP- and IR780-loaded nanoparticles were observed by TEM to be uniform spheres approximately 150 nm in diameter (Fig. 4D), consistent with the results obtained by DLS (Fig. 4E). CIP- and IR780-loaded nanoparticles (termed P_{2000}S-NP@CIP and P_{2000}S-NP@IR780, respectively) were prepared at the same time (Table S5). Examination of the UV–vis–NIR spectra of the nanoparticles (Fig. 4F) showed that the absorption peak of P_{2000}S-NP@(C + I) was similar to that of IR780, with maximum absorption at approximately 782 nm. To confirm the stability of P_{2000}S-NP@(C + I) in various media, the nanoparticle sizes were determined in water, PBS (pH 7.4), normal saline (NS), and BHI medium as a function of time (Fig. 4G). The results showed that the drug-loaded nanoparticles displayed excellent size stability in PBS, NS, and BHI medium and that the particle size increased slightly in water. MTT assays were further performed to evaluate the biocompatibility of drug-free and drug-loaded nanoparticles. As shown in Fig. S8, no cytotoxicity was observed among those nanoparticles analyzed against NIH 3T3 cells, suggesting that the PEG-decorated and glycocalyx-mimicking nanoparticles have good biocompatibility and that they show great potential for application in drug delivery to eradicate oral biofilms (details showed in supporting information).

3.5. pH-dependent in vitro CIP release

The above results confirmed that the nanoparticles underwent dissociation due to the hydrolysis of the ortho esters under acidic conditions (pH 4.7), which was characterized by an increase in particle size and destruction of their shape as viewed by TEM. To demonstrate the

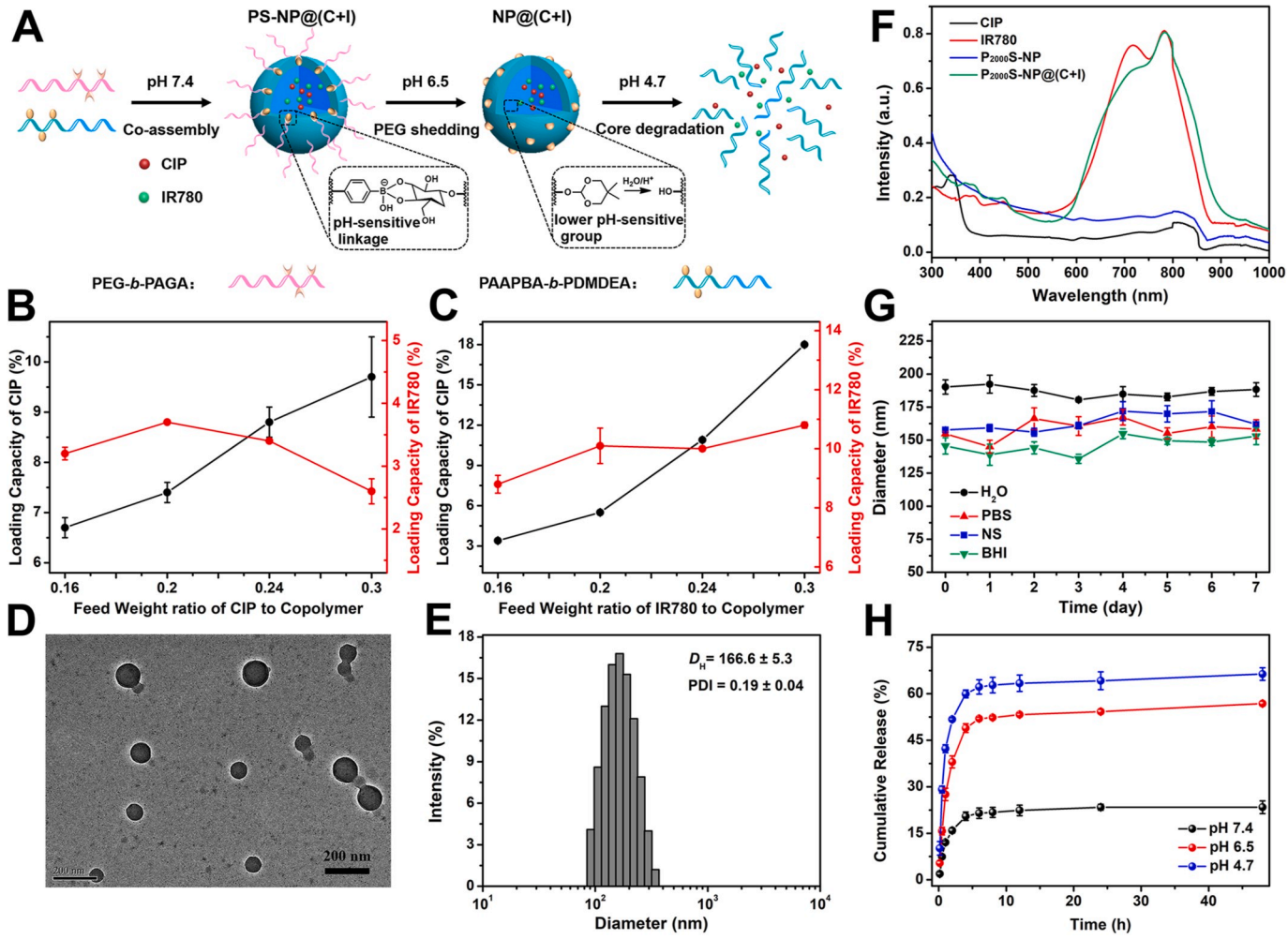

Fig. 4. (A) Schematic illustration of the PS-NP@(C + I) formulation; (B) Loading capacity of CIP and IR780 as a function of the feed weight ratio of CIP to the copolymer when the feed weight ratio of IR780 to the copolymer is 0.16; (C) Loading capacity of CIP and IR780 as a function of the feed weight ratio of IR780 to the copolymer when the feed weight ratio of IR780 to the copolymer is 0.24; (D) TEM image and (E) size distribution of P_{2000}S-NP@(C + I); (F) UV–vis–NIR spectra of CIP, IR780, P_{2000}S-NP, and P_{2000}S-NP@(C + I); (G) change in the diameter of P_{2000}S-NP@(C + I) over time in various media; (H) Cumulative *in vitro* release of CIP from P_{2000}S-NP@(C + I) as a function of pH.

pH-responsive drug release behavior of the nanoparticles, *in vitro* CIP release experiments were performed with P_{2000}S-NP@(C + I) at different pH values (7.4, 6.5, and 4.7). As shown in Fig. 4H, only 23% of the CIP was released from P_{2000}S-NP@(C + I) after 48 h incubation in PBS at pH 7.4. However, when the pH was decreased to 6.5, the drug released during the same period increased to nearly 57%, and almost 49% of the loaded drug was released within 4 h. It could be speculated that the weakly acidic conditions induced dissociation of the boronate ester bonds and detachment of the PEG shell, resulting in the free diffusion of drugs from the core. At pH 4.7, the drug release was further accelerated compared with that at pH 6.5, resulting in a cumulative release of 49% during the initial 4 h and release of 67% of the drug after 48 h. This occurred mainly due to detachment of the PEG shell under the slightly acidic conditions and hydrolysis of the ortho-esters in the core at the lower pH, leading to complete dissociation of the nanoparticles and an overall rapid drug release. The above results demonstrate the oral biofilm microenvironment-responsive drug release pattern of the newly prepared drug vehicle.

3.6. Antimicrobial efficacy

The photodynamic and photothermal properties of P_{2000}S-NP@(C + I) under NIR laser irradiation (808 nm, 1.5 W/cm^2) were determined by using the 2′,7′-dichlorodihydrofluorescein diacetate (DCFH-DA) method and measuring the increase of temperature (see the supporting information, Figs. S9 and S10). We further evaluated the antimicrobial efficacy of NIR-activated nanoplatforms against planktonic *S. mutans* using a bacterial growth inhibition assay. The bacterial suspension was treated with the antibacterial samples for 2 h, irradiated with a NIR laser (808 nm, 1.5 W/cm^2) for 5 min, and incubated for an additional 8 h to permit the growth of bacteria. Bacteria treated with PBS were used as a negative control to define a bacterial survival of 100%. As shown in Fig. 5A, P_{2000}S-NP@CIP inhibited *S. mutans* more significantly than that of the same dosage of free CIP. Considering that the blank carriers (P_{2000}S-NP) showed negligible inhibition against *S. mutans* (Fig. S13A), a conclusion could be drawn that the obtained nanovehicles greatly enhanced the antibacterial activity of CIP. Notably, NIR irradiation alone was unable to inhibit the growth of bacteria. However, the efficacy of bacterial killing by P_{2000}S-NP@IR780 was only initiated upon NIR irradiation; under these conditions, toxic ROS and hyperthermia produced by the irradiation destroyed the bacteria. In addition, at the same concentration of CIP or IR780, the antibacterial effect of NIR-activated P_{2000}S-NP@(C + I) was better than that of P_{2000}S-NP@CIP or P_{2000}S-NP@IR780 under NIR irradiation; the MIC for CIP decreased from 1.73 to 0.87 μg/mL, and that for IR780 decreased from 1.88 to 0.94 μg/mL. The effect of irradiation time on the antibacterial properties of P_{2000}S-NP@IR780 and

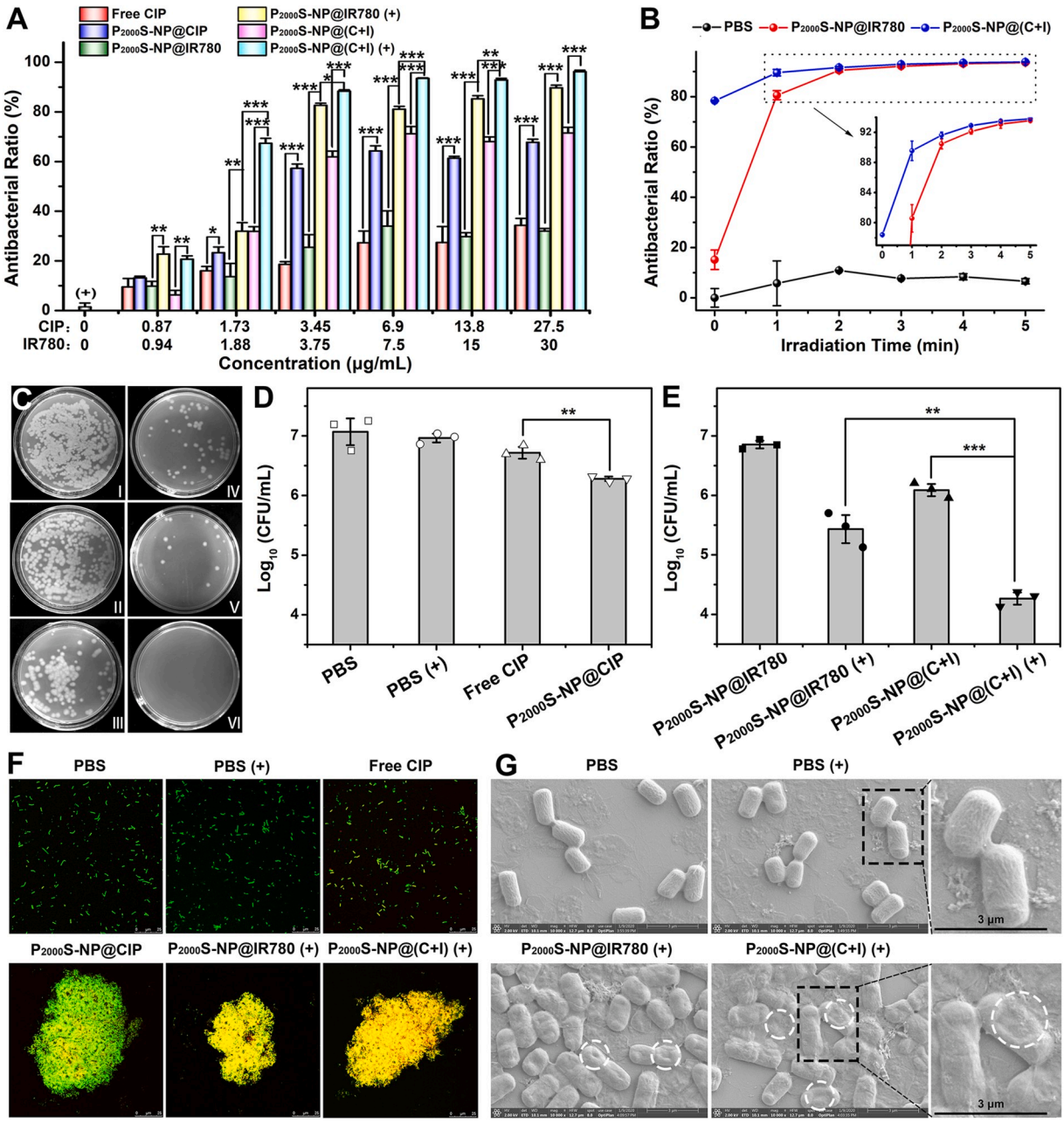

Fig. 5. (A) *In vitro* antibacterial effects of various materials with various drug dosage concentrations against *S. mutans*. (B) *In vitro* antibacterial effect of P_{2000}S-NP@IR780 and P_{2000}S-NP@(C + I) as a function of NIR laser irradiation (808 nm, 1.5 W/cm^2) time. (C) Photographs of BHI plate colonies of *S. mutans* suffering from different treatments. I, PBS; II, PBS (+); III, free CIP; IV, P_{2000}S-NP@CIP; V, P_{2000}S-NP@IR780 (+); VI, P_{2000}S-NP@(C + I) (+). (D) and (E) Quantitative results showing the bacterial CFUs in each group by BHI plate counting. Each experiment was performed in triplicate, and the results were reported as mean ± s.d. (F) CLSM images of *S. mutans* stained with AO (green, live cells) and EB (red, dead cells) in different groups. All of the materials were applied at uniform dosages of CIP (55 μg/mL) and IR780 (60 μg/mL). (G) SEM images of *S. mutans* after treatment with different groups. White circles indicate morphological damage to bacterial cells.

P_{2000}S-NP@(C + I) against *S. mutans* was further analyzed. As shown in Fig. 5B, no antimicrobial activity was observed in the PBS group regardless of the duration of exposure. The antibacterial activities of P_{2000}S-NP@IR780 and P_{2000}S-NP@(C + I) gradually increased as the irradiation time was extended, indicating that the light-activated antibacterial effect of IR780 occurred in a time-dependent manner, consistent with the time dependence of the photothermal/photodynamic performance of IR780. Notably, P_{2000}S-NP@(C + I) showed slightly better light-activated antimicrobial efficacy than P_{2000}S-NP@IR780 under the same conditions (inset in Fig. 5B), highlighting the additive effects of CIP and IR780. The Standard plate counting method was employed to further investigate the antibacterial activity of P_{2000}S-NP@(C + I) under NIR irradiation (Figs. S13B and S13C, Fig. 5C–E). From the results, nearly 95% of bacterial cells were killed by P_{2000}S-NP@IR780 upon NIR irradiation. In contrast, NIR-irradiated P_{2000}S-NP@(C + I) exhibited the most striking antibacterial efficacy: almost no bacterial colonies were found in the plate, representing a killing rate of 99.8%. The results indicate that the remarkable antibacterial ability of P_{2000}S-NP@(C + I) is attributable to the combined effects of IR780-mediated photothermal and photodynamic therapy as well as to the virulence function of CIP at moderate doses.

The *in vitro* antibacterial behavior of light-activated nanoplatforms against *S. mutans* was further determined using LIVE/DEAD fluorescent staining assays (Fig. 5F and Fig. S13D). When treated with PBS,

regardless of light irradiation, the bacteria were scattered, and the majority of the bacteria appeared green, indicating survival. In contrast, the nanoparticle-treated bacteria aggregated into large clusters that were labeled with obvious green fluorescence, and yellow signals overlying green and red increased gradually in the P_{2000}S-NP@CIP, NIR-irradiated P_{2000}S-NP@IR780 and NIR-irradiated P_{2000}S-NP@(C + I) groups, implying the most significant antibacterial activity of NIR-irradiated P_{2000}S-NP@(C + I) against *S. mutans*. SEM imaging was harvested to observe changes of bacterial morphologies after treatment with the nanoplatforms under NIR irradiation (Fig. 5G and Fig. S13E). SEM images of bacterial cells in control groups (PBS and PBS (+)) showed smooth surfaces and integrated structures. In contrast, the cell wall of bacteria treated with P_{2000}S-NP@IR780 or P_{2000}S-NP@(C + I) upon NIR irradiation was observed to be seriously damaged and present irregularly shaped holes. The above results imply that the combined antibacterial effects of P_{2000}S-NP@(C + I) and NIR irradiation can be employed to treat oral bacteria.

3.7. Biofilm penetration of PEGylated nanoplatforms

To validate the PEG-reinforced penetration and accumulation of nanoparticles in biofilms, freshly formed *S. mutans* biofilms were

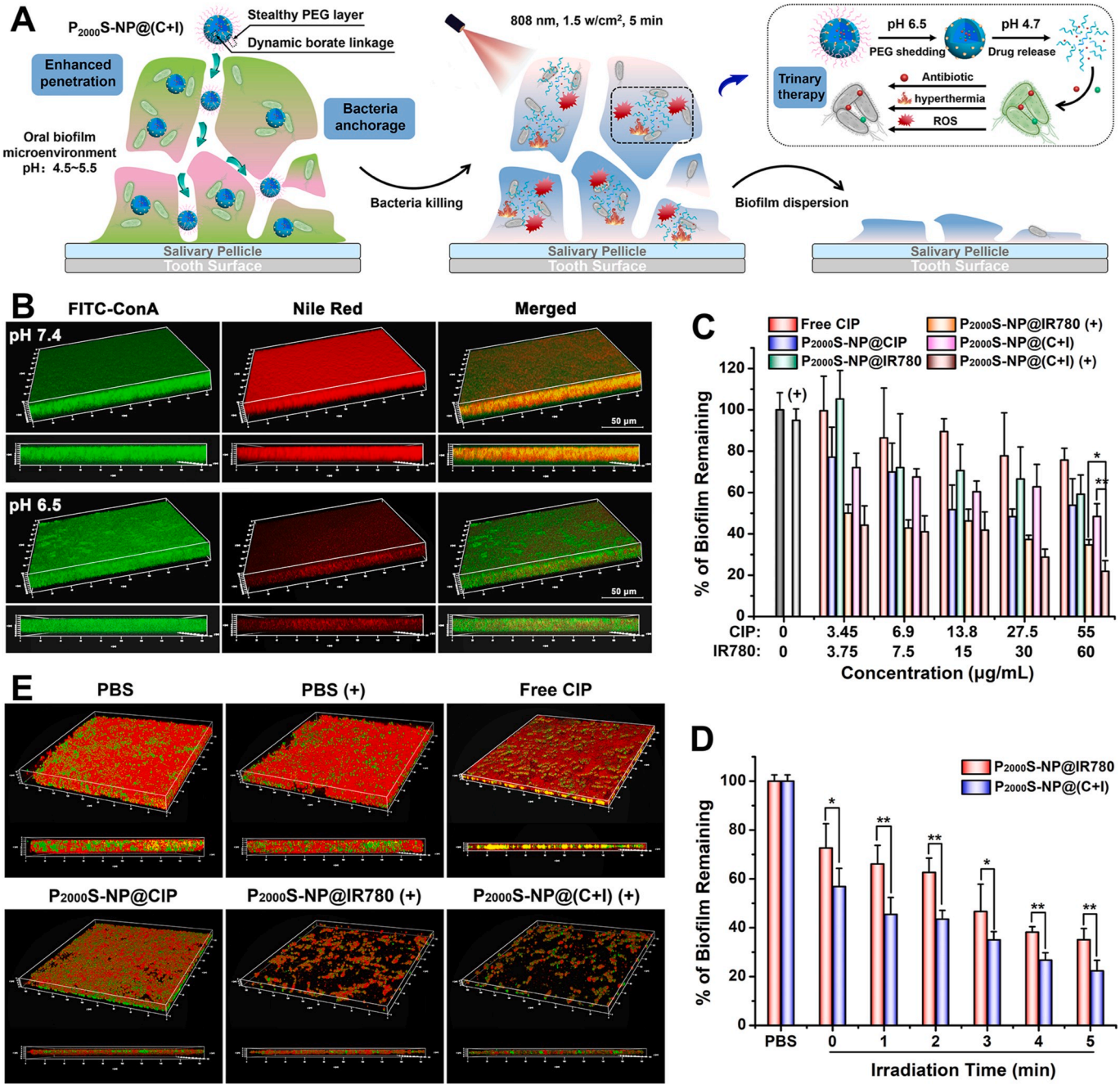

Fig. 6. (A) Schematic diagram of the self-modulating nanoplatform that uses biofilm penetration and bacterial anchorage to enhance oral biofilm dispersion under trinary therapy. (B) 3D-CLSM images showing the penetration and accumulation of P_{2000}S-NP@NIL in *S. mutans* biofilms at pH 7.4 and pH 6.5; green fluorescence: biofilm EPS labeled with FITC-ConA. (C, D) Percentage of *S. mutans* biofilm remaining after different treatments as a function of concentration (C) and 808 nm laser irradiation (1.5 W/cm^2) time (D). The results were reported as mean ± s.d. ($n = 5$). (E) CLSM 3D images of *S. mutans* biofilms in various groups. Red: bacterial cells stained with EB; green: biofilm EPS labeled with FITC-ConA. All applied materials were used at a uniform dosage of CIP (55 μg/mL) or IR780 (60 μg/mL).

exposed to suspensions of Nile red-loaded PEGylated nanoplatforms (P_{2000}S-NP@NIL) and imaged using CLSM 3D. At pH 7.4, Nile red loaded in P_{2000}S-NP@NIL penetrated the *S. mutans* biofilms well, shown by the fact that evident red fluorescence was uniformly distributed within the biofilm at some positions, even reaching the bottom of the biofilm (top of Fig. 6B). However, demonstrable penetration and accumulation of P_{2000}S-NP@NIL in the biofilm obviously declined at pH 6.5 (lower part of Fig. 6B), suggesting that biofilm penetration was limited when the PEG layer was shed from the nanoplatform under a weakly acidic biofilm microenvironment. Quantitative analysis of the red fluorescence intensity across the thickness of the *S. mutans* biofilm indicated that the penetration and accumulation of P_{2000}S-NP@NIL in the biofilm was more significant at pH 7.4 (Fig. S14A) than at pH 6.5 (Fig. S14B). Evidently, the negatively charged surface and "stealthy" PEGylated shell contribute to the low affinity of the nanoplatform to the biofilm matrix, allowing its deep penetration into the biofilm and accumulation of demonstrable concentrations of Nile red-loaded nanoplatforms [18,25,26].

3.8. Antibiofilm activity

Bacterial biofilms, which are inherently resistant to antibiotics due to their decreased membrane permeability and acidic microenvironment, play significant roles in diverse chronic bacterial infections. From Fig. S15, obvious low pH was observed in mature *S. mutans* biofilm, which could be used as a target for the application of a pH-activated therapeutic nanoplatform. To determine the antibiofilm activity of the self-modulating microenvironment-activated nanoplatforms against *S. mutans* under trinary therapy (Fig. 6A), the mature biofilms were treated with various samples at a variety of concentrations with or without 808 nm NIR irradiation (1.5 W/cm^2). Quantification of the remaining biofilm was performed using the classical crystal violet method. Fig. 6C and Fig. S16 show the dispersion percentages of *S. mutans* biofilms treated with the antibacterial materials as a function of concentration. It was observed that free CIP exhibited negligible efficacy in eradicating biofilms. In contrast, the biofilm dispersion rate of P_{2000}S-NP@CIP reached 40–50%, demonstrating an evident improvement in the antibiofilm ability of CIP upon encapsulation into PEGylated nanoplatforms with reinforced biofilm penetration and programmed bacteria targeting. In addition, P_{2000}S-NP@IR780 and NIR-irradiated P_{2000}S-NP@(C + I) achieved considerably high biofilm dispersion percentages of 60%–70% and 70%–80%, respectively, under 808 nm irradiation. The comparatively greater antibiofilm activity of NIR-irradiated P_{2000}S-NP@(C + I) compared to P_{2000}S-NP@CIP and NIR-irradiated P_{2000}S-NP@IR780 indicates the existence of combined antibiofilm effects between the loaded CIP and IR780. We further evaluated the dispersing action of P_{2000}S-NP@IR780 and P_{2000}S-NP@(C + I) on *S. mutans* biofilms as a function of irradiation time. As shown in Fig. 6D, both P_{2000}S-NP@IR780 and P_{2000}S-NP@(C + I) showed irradiation time-dependent antibiofilm effects. In particular, P_{2000}S-NP@(C + I) displayed better dispersion capability than P_{2000}S-NP@IR780 after the same irradiation time, yielding a striking reduction in biofilms reaching 40%–50% upon 808 nm NIR irradiation (1.5 W/cm^2) for only 1 min. We envision that the excellent light-driven antibiofilm activity of P_{2000}S-NP@(C + I) is conceivably the result of enhanced biofilm penetration by PEGylation, efficient PBA-mediated bacterial localization, microenvironment-responsive drug release and combined bacterial killing between antibiotics and IR780-mediated PTT/PDT.

3.9. CLSM 3D observation

To visualize the dispersing performance of the PEG-sheddable microenvironment-responsive nanoplatforms under NIR irradiation toward *S. mutans* biofilms, the treated biofilms were stained simultaneously with FITC-ConA and EB to localize the polysaccharide matrix and dead bacterial cells within the biofilms and observed by CLSM 3D imaging (Fig. 6E and Fig. S17). Compared with the control groups (PBS and PBS plus irradiation), the biofilms treated with free CIP maintained a relatively intact structure with dense bacteria in the internal space, suggesting a negligible antibiofilm effect of the drug alone due to its low biofilm penetration. As expected, the dispersion activity of CIP encapsulated into the PEGylated nanoplatform against biofilms was significantly enhanced compared with that of free CIP, presumably due to the improved deep penetration into biofilms and alterable active targeting to the inner bacteria under the shell detachment strategy. In addition, after treatment with P_{2000}S-NP@CIP, NIR-irradiated P_{2000}S-NP@IR780 or NIR-irradiated P_{2000}S-NP@(C + I), the biofilms were destroyed to varying degrees, with reduced EPS and bacteria remaining in the biofilms. In particular, NIR-irradiated P_{2000}S-NP@(C + I) displayed more obvious destruction than P_{2000}S-NP@IR780 and NIR-irradiated P_{2000}S-NP@IR780, indicating combined antibiofilm effects of the antibiotic and IR780-mediated PTT/PDT. As a result, with the aid of PEG-reinforced biofilm penetration, re-exposure of PBA ligands for bacterial targeting upon shell detachment in response to slightly acidic conditions, microenvironment-responsive drug release, and the additive action of CIP and IR780, light-activated P_{2000}S-NP@(C + I) displayed excellent dispersing activity against *S. mutans* biofilms under 808 nm NIR irradiation.

3.10. Disruption of ex vivo biofilms

To gain further insight into the therapeutic potential of the obtained nanoplatform, an *ex vivo* human biofilm model was used to assess whether P_{2000}S-NP@(C + I) plus NIR irradiation can eradicate cariogenic biofilms. The excised human teeth received from volunteers in Tianjin Stomatological Hospital were processed to remove the root and retain the crown, and then infected with *S. mutans* or *L.acidopilus* biofilm and treated with the nanoparticles and/or NIR irradiation (808 nm, 1.5 W/cm^2) for 5 min. The remaining biofilms were observed and quantified by using the crystal violet method. As shown in Fig. S18, the nanomaterials exhibited similar eradication effects against both kinds of cariogenic biofilms. Briefly, it was observed that the biofilm dispersion rate of P_{2000}S-NP@CIP reached 40–55% while NIR-irradiated P_{2000}S-NP@IR780 and NIR-irradiated P_{2000}S-NP@(C + I) achieved considerably high percentages in biofilm dispersion of 60–70% and 80–85%, respectively. As a result, the prepared P_{2000}S-NP@(C + I) under NIR irradiation can effectively eradicate both *S. mutans* or *L.acidopilus* biofilms *ex vivo*, indicating the broad-spectrum efficacy against cariogenic biofilms.

3.11. In vivo suppression of dental caries

We further sought to determine the *in vivo* efficacy of P_{2000}S-NP@(C + I) under NIR irradiation on the suppression of oral biofilm-associated infections using a well-established rodent model that simulates the features of early childhood severe caries, including *S. mutans* infection, in rat pups and long-term feeding on a sugar-rich diet. Upon the successful establishment of the *S. mutans*-infected rat rodent model (Figs. S19A and 19B) and after grouping the rats (PBS (+), free CIP, P_{2000}S-NP@CIP, P_{2000}S-NP@IR780 (+), and P_{2000}S-NP@(C + I) (+)), we topically administered the corresponding materials by oral swabs with or without light irradiation every other day (Fig. 7A). To validate the biofilm penetrating ability of prepared nanoplatforms *in vivo*, freshly formed *S. mutans* biofilms growing on the teeth of rat pup were exposed to suspensions of Nile red-loaded PEGylated nanoplatforms (P_{2000}S-NP@NIL) for 15 min, stained with FITC-ConA to label EPS, and then imaged using CLSM 3D. As shown in Fig. S19C, evident red fluorescence from Nile red was uniformly distributed within the biofilm from top to the bottom, implying that the nanoplatforms can effectively penetrate the cariogenic biofilms *in vivo* within 15 min of a spacing interval before NIR irradiation. Using this therapeutic schedule, we were able to evaluate the incidence and severity of caries lesions in the teeth of the rat

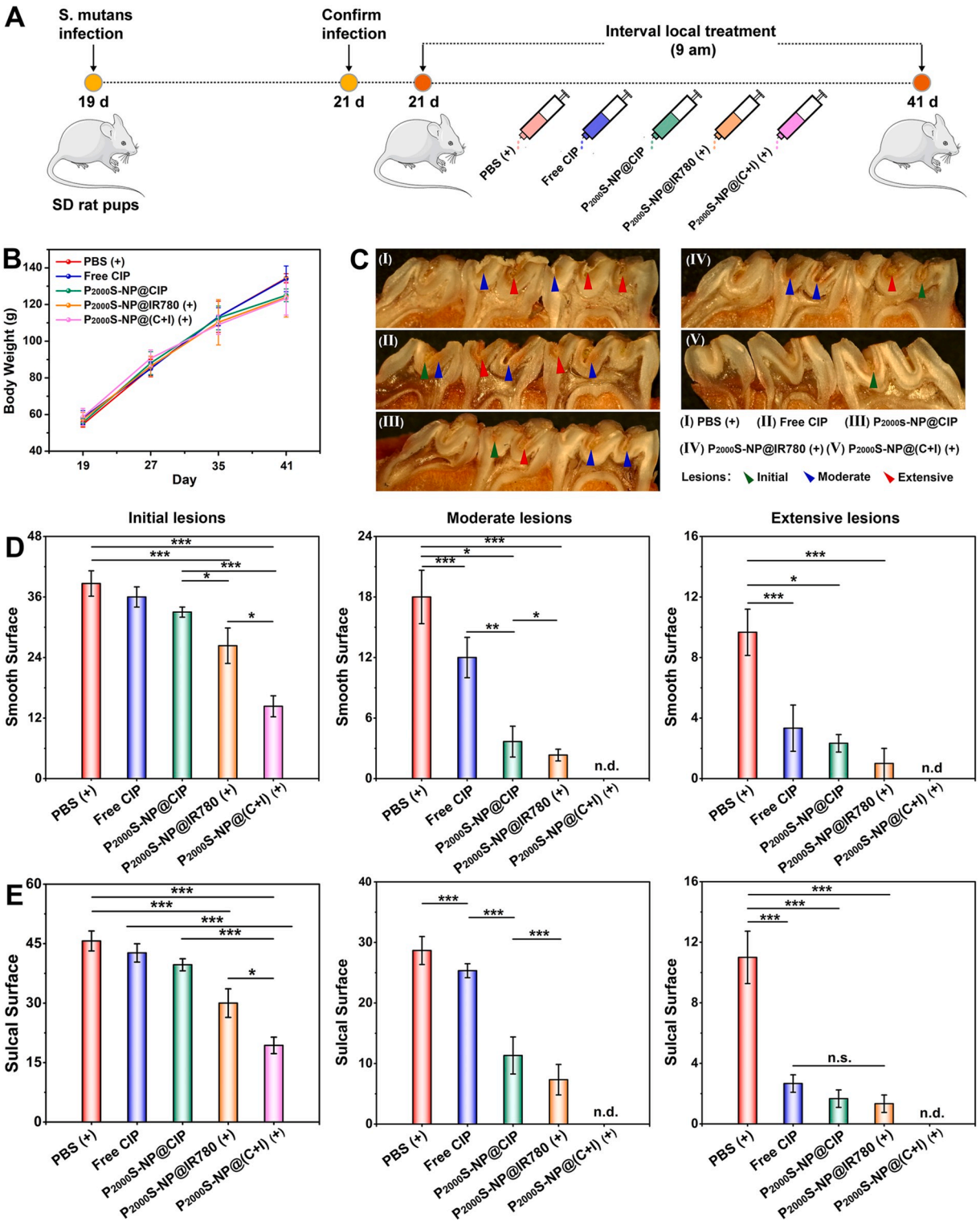

Fig. 7. (A) Experimental design and treatment regimen. (B) Body weights of rat pups during the experimental period. (C) Images of rat teeth after treatment. Green arrows indicate initial lesions where the enamel is demineralized; blue arrows indicate moderate lesions where the enamel is damaged; red arrows indicate the most severe carious lesions where the enamel is eroded leading to cavitation. (D–E) Caries onset and severity of smooth (D) and sulcal surfaces (E). Caries scores are recorded as stages and extent of carious lesion severity according to Larson's modification of Keyes' scoring system. The data are presented as the mean ± s.d. ($n = 6$). $^{*}P < 0.05$, $^{**}P < 0.01$, $^{***}P < 0.001$; n.d., not detectable; n.s., nonsignificant.

pups. During the 21-day treatment period, there were no significant differences in the body weights of the rats in the various test groups, implying that the treated rats all maintained obvious good health (Fig. 7B).

In this model, tooth enamel gradually formed carious lesions that proceeded from initial areas of enamel demineralization (green arrow) to moderate lesions (blue arrows) and ultimately to extensive (severe) lesions characterized by enamel structure damage and cavitation (red arrow, Fig. 7C). Quantitative caries scoring analyses (Fig. 7D and E) showed that P_{2000}S-NP@CIP partially attenuated the initiation and

severity of carious lesions compared with PBS (+) and free CIP, potentially benefiting from the enhanced drug bioavailability due to the flexible modulation of biofilm infiltration and bacterial attachment. Furthermore, the efficacy of dual therapy with P_{2000}S-NP@(C + I) under light irradiation was considerably better than that of P_{2000}S-NP@CIP or P_{2000}S-NP@IR780 (+); it decreased the number of carious lesions more efficaciously, significantly prevented extensive enamel damage, and circumvented the development of cavitation on both the smooth and sulcal surfaces, thereby demonstrating a combined therapeutic effect of CIP and IR780 under NIR irradiation. The above results demonstrate that topical administration of NP_{2000}@(C + I) plus light irradiation can efficaciously inhibit the development of dental caries at both dental surfaces. Hematoxylin and eosin (H&E) stained photographs of gingival and palatal tissues from the treated rats showed no inflammatory responses, proliferative changes, or necrosis (Fig. 8), demonstrating good biocompatibility of the nanoplatforms and an irradiation period of 808 nm NIR. The results suggest that topical treatment with a self-modulating nanosystem plus light irradiation can efficaciously prevent the development of prevalent biofilm-associated dental caries *in vivo* with no adverse effects on peripheral soft tissues.

4. Discussion

The obtained data provide direct evidence of a NIR-assisted treatment strategy for effective dispersion of oral biofilms and prevention of severe tooth decay under a topical treatment regimen. The strategy is involved with a well-orchestrated polymeric nanoplatform that serves as a carrier to facilitate topical delivery of antibiotics and phototherapeutic agents into oral biofilms. The nanoplatform armed with a "stealthy" PEG layer lathered to PBA block through dynamic borate linkage can favorably penetrate EPS into biofilms whereas suffering from PEG detachment under the weakly acidic biofilm microenvironment to re-expose PBA ligands for bacteria targeting, which provides a versatile approach to coordinate the functionalities of biofilm penetration and bacteria anchorage for self-regulated targeted anti-biofilm drug delivery. Importantly, the nanoplatform can be further activated by the specific acidic pH values found in cariogenic biofilms to "on-site" release the encapsulated cargoes for bacteria killing under three-in-one action of antibiotics, hyperthermia and cytotoxic ROS upon exposure to NIR irradiation, thus ultimately disrupting the hard-eradicating oral biofilms. Such properties thwarted cariogenic biofilm accumulation and prevented the onset of severe dental caries with no adverse events in the fitness of surrounding tissues *in vivo*. The application of the current therapeutic strategy can be extended to other types of oral biofilm infectious diseases since acidic microenvironment can be found in other pathological conditions, such as dental plaque [49] and periodontitis [18,50,51]. Thus, the exploitation of microenvironment-actuated phototherapy approach could open up a new road for the treatment of severe infectious diseases.

As known, impotent penetration of antimicrobial drugs into dense biofilms remains the leading challenge of anti-biofilm treatments, which propels the development of PEG-based EPS-penetrable drug conjugate or nanocarrier for effective drug penetration into biofilms [18,24,25]. Besides, the high drug bioavailability serves as another prerequisite of efficient bacteria killing that impacts overall biofilm dispersion, allowing for bacterial anchorage followed by "on-site" drug release could be a feasible strategy to improve drug bioavailability within biofilms [18]. To date, however, little research has focused on the collaboration of the two sides to optimize anti-biofilm drug delivery despite the strides of anti-biofilm therapy. Our current research aims to address the contradiction of PEG between reinforced biofilm penetration and low affinity for bacteria, providing a general strategy to coordinate biofilm penetration and bacteria anchorage in a self-modulating manner for efficacious anti-biofilm drug delivery.

Additionally, non-invasive phototherapy is proposed in this study to synergy with antibiotics for NIR-controlled biofilm eradication and prevention of infectious diseases. From the results, the topical administration of prepared nanoplatforms plus NIR irradiation yielded an excellent antibiofilm efficacy *in vitro* and *in vivo*, which was more significant than that of the free antibiotics. This system could efficiently prevent the onset of biofilm-associated dental caries with no adverse effects on peripheral soft tissues, indicating a promising future in oral application. As known, phototherapy has recently aroused the researchers' interest in oral diseases due to the robust bacterial killing performance of hyperthermia [52] and light-activated ROS [49–51]. Considering that NIR-assisted therapy with comparable superiority not to induce bacterial resistance, the combination of antibiotics and PDT/PTT could be an innovative treatment method for oral health care despite a 5 min of light irradiation was needed compared to routine oral treatment. Particularly worth mentioning is the time of NIR application, 5 min was a suitable period for treatment of mice but maybe not acceptable for human treatment. The optimal time of NIR exposition for practical use should be further investigated and regulated in the future, maybe a regimen of multiple short bursts of light is recommended. We

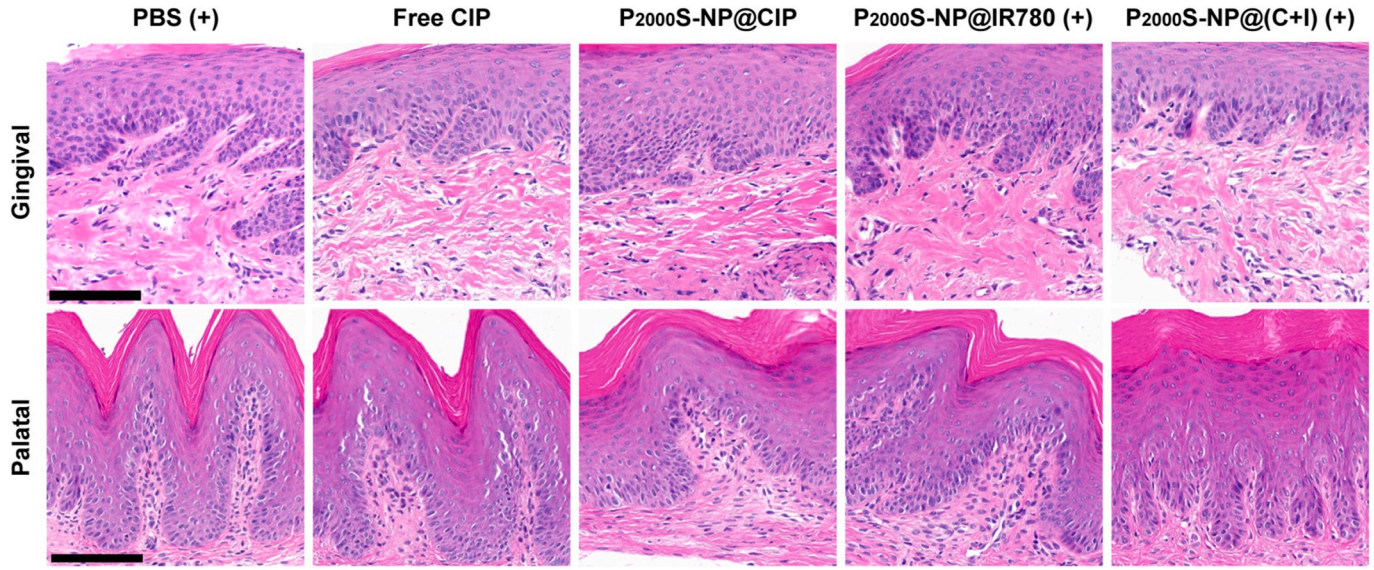

Fig. 8. Histopathology of gingival and palatal tissue in rats in the different groups (scale bar: 50 μm).

consider that the light-guided therapeutic regimen in the present work could be feasible and practical if the illumination device, irradiation time and power are optimized roundly in the following investigations.

5. Conclusion

In summary, we have developed a biofilm microenvironment-modulated nanoplatform for targeted drug delivery to combat drug-resistant oral biofilm-associated infections. This novel strategy involves the utilization of dynamic covalent chemistry to address the contradiction between EPS penetration and bacterial targeting in biofilm drug delivery. The "stealthy" corona is retained in the system to maintain stability and biocompatibility and to allow enhanced deep penetration into oral biofilms. After the nanoplatform reaches and accumulates within the biofilms, the slight acidity of the biofilm triggers the rapid detachment of the "stealthy" shell and exposes the targeting ligands for bacterial localization. The sheddable system is then subjected to dissociation in response to the acidic biofilm microenvironment and achieves "on-demand" drug release at bacteria-specific sites. Self-regulated nanoplatforms involving multimodal bacterial killing suppress the evolution of oral biofilms and severe tooth decay *in vivo* in a rodent model of the disease. Consequently, these merits of the nanoplatform system, as well as the near-infrared light-driven activity, impart great inhibition efficacy against oral biofilms compared with drugs alone. Accordingly, this versatile system provides a promising strategy for difficult-to-treat oral biofilm infections.

Author contributions

Nankai University: Xinge Zhang and Yunjian Yu designed the project and wrote the manuscript, Yunjian Yu performed most of the experiments, Yufei Zhang carried out the animal experiments. Yijie Cheng, Haonan Sun, Xiaosong Wei, Zhuang Ma, Jie Li, and Yayun Bai help the data processing and manuscript proofreading. Tianjin Medical University: Zhongming Wu discussed the project and gave help in the *in vivo* study. Tianjin Stomatological Hospital: Yuxia Wang, and Zeyuan Chen participated in the animal experiments from feasibility evaluation to caries scoring and histopathological analysis.

Data availability statement

The data that support the findings of this study are available from the corresponding author upon reasonable request.

CRediT authorship contribution statement

Yunjian Yu: Term, Conceptualization, Methodology, Software, Formal analysis, Investigation, Data curation, Writing – original draft, preparation. **Yufei Zhang:** Formal analysis, Investigation, Resources, Data curation, Writing – review & editing. **Yijie Cheng:** Investigation, Resources. **Yuxia Wang:** Resources, Visualization, Investigation. **Zeyuan Chen:** Resources, Visualization, Investigation. **Haonan Sun:** Software, Investigation. **Xiaosong Wei:** Supervision. **Zhuang Ma:** Software. **Jie Li:** Visualization. **Yayun Bai:** Supervision. **Zhongming Wu:** Term, Writing – review & editing, Project administration, Funding acquisition. **Xinge Zhang:** Term, Conceptualization, Writing – original draft, Writing – review & editing, Supervision, Project administration, Funding acquisition.

Declaration of competing interest

The authors declare no conflict of interest.

Acknowledgements

This work was supported by National Natural Science Foundation of China (Grant No. 21975133, 21774062), and the Key Projects of Natural Science Foundation of Tianjin, China (19JCZDJC36900). This work is dedicated to the 100th anniversary of Chemistry at Nankai University.

Appendix A. Supplementary data

Supplementary data to this article can be found online at https://doi.org/10.1016/j.bioactmat.2021.10.035.

References

[1] J.L. Del Pozo, R. Patel, The challenge of treating biofilm-associated bacterial infections, Clin. Pharmacol. Ther. 82 (2007) 204–209.
[2] K. Lewis, Persister cells, dormancy and infectious disease, Nat. Rev. Microbiol. 5 (2007) 48–56.
[3] T.F. Flemmig, T. Beikler, Control of oral biofilms, Periodontol. 2000 55 (2011) 9–15.
[4] R.P.J. Allaker, The use of nanoparticles to control oral biofilm formation, Dent. Res. 89 (2010) 1175–1186.
[5] H.-C. Flemming, J. Wingender, The biofilm matrix, Nat. Rev. Microbiol. 8 (2010) 623–633.
[6] O. Fejerskov, A.A. Scheie, F. Manji, The effect of sucrose on plaque pH in the primary and permanent dentition of caries-inactive and -active kenyan children, J. Dent. Res. 71 (1992) 25–31.
[7] N. Takahashi, B. Nyvad, Caries ecology revisited: microbial dynamics and the caries process, Caries Res. 42 (2008) 409–418.
[8] W.H. Bowen, The stephan curve revisited, Odontology 101 (2013) 2–8.
[9] Y. Li, R.A. Burne, Regulation of the gtfBC and ftf genes of Streptococcus mutans in biofilms in response to pH and carbohydrate, Microbiology 147 (2001) 2841–2848.
[10] D. Davies, Understanding biofilm resistance to antibacterial agents, Nat. Rev. Drug Discov. 2 (2003) 114–122.
[11] D. Lebeaux, J.M. Ghigo, C. Beloin, Biofilm-related infections: bridging the gap between clinical management and fundamental aspects of recalcitrance toward antibiotics, Microbiol. Mol. Biol. Rev. 78 (2014) 510–543.
[12] D.S. Benoit, H. Koo, Targeted, triggered drug delivery to tumor and biofilm microenvironments, Nanomedicine 11 (2016) 873–879.
[13] T.O. Peulen, K.J. Wilkinson, Characterization and optimization of pH-responsive polymer nanoparticles for drug delivery to oral biofilms, Environ. Sci. Technol. 45 (2011) 3367–3373.
[14] D.S.W. Benoit, K.R. Sims, D. Fraser, Nanoparticles for oral biofilm treatments, ACS Nano 13 (2019) 4869–4875.
[15] B. Horev, M.I. Klein, G. Hwang, Y. Li, D. Kim, H. Koo, D.S.W. Benoit, pH-Activated nanoparticles for controlled topical delivery of farnesol to disrupt oral biofilm virulence, ACS Nano 9 (2015) 2390–2404.
[16] X. Xu, L. He, B. Zhu, J. Li, J. Li, Advances in polymeric materials for dental applications, Polym. Chem. 8 (2017) 807–823.
[17] Z. Zhao, C. Ding, Y. Wang, H. Tan, J. Li, pH-responsive polymeric nanocarriers for efficient killing of cariogenic bacteria in biofilms, Biomater. Sci. 7 (2019) 1643–1651.
[18] Y. Xi, Y. Wang, J. Gao, Y. Xiao, J. Du, Dual corona vesicles with intrinsic antibacterial and enhanced antibiotic delivery capabilities for effective treatment of biofilm-induced periodontitis, ACS Nano 13 (2019) 13645–13657.
[19] X. Pang, Q. Xiao, Y. Cheng, E. Ren, L. Lian, Y. Zhang, H. Gao, X. Wang, W. Leung, X. Chen, G. Liu, C. Xu, Bacteria-responsive nanoliposomes as smart sonotheranostics for multidrug resistant bacterial infections, ACS Nano 13 (2019) 2427–2438.
[20] Z. Zhou, F. Hu, S. Hu, M. Kong, C. Feng, Y. Liu, X. Cheng, Q. Ji, X. Chen, pH-Activated nanoparticles with targeting for the treatment of oral plaque biofilm, J. Mater. Chem. B 6 (2018) 586–592.
[21] K. Forier, K. Raemdonck, S.C. De Smedt, J. Demeester, T. Coenye, K. Braeckmans, Lipid and polymer nanoparticles for drug delivery to bacterial biofilms, J. Contr. Release 190 (2014) 607–623.
[22] J.M. Harris, R.B. Chess, Effect of pegylation on pharmaceuticals, Nat. Rev. Drug Discov. 2 (2003) 214–221.
[23] M.E. Davis, Z. Chen, D.M. Shin, Nanoparticle therapeutics: an emerging treatment modality for cancer, Nat. Rev. Drug Discov. 7 (2008) 771–782.
[24] J. Du, H.M.H.N. Bandara, P. Du, H. Huang, K. Hoang, D. Nguyen, S.V. Mogarala, H. D.C. Smyth, Improved biofilm antimicrobial activity of polyethylene glycol conjugated tobramycin compared to tobramycin in Pseudomonas aeruginosa biofilms, Mol. Pharm. 12 (2015) 1544–1553.
[25] Y. Liu, H.J. Busscher, B. Zhao, Y. Li, Z. Zhang, H.C. van der Mei, Y. Ren, L. Shi, Surface-adaptive, antimicrobially loaded, micellar nanocarriers with enhanced penetration and killing efficiency in Staphylococcal biofilms, ACS Nano 10 (2016) 4779–4789.
[26] S. Tian, L. Su, Y. Liu, J. Cao, G. Yang, Y. Ren, F. Huang, J. Liu, Y. An, H.C. van der Mei, H.J. Busscher, L. Shi, Self-targeting, zwitterionic micellar dispersants enhance antibiotic killing of infectious biofilms-An intravital imaging study in mice, Sci. Adv. 6 (2020), eabb1112.
[27] Y. Liu, P.C. Naha, G. Hwang, D. Kim, Y. Huang, A. Simon-Soro, H.-I. Jung, Z. Ren, Y. Li, S. Gubara, F. Alawi, D. Zero, A.T. Hara, D.P. Cormode, H. Koo, Topical ferumoxytol nanoparticles disrupt biofilms and prevent tooth decay in vivo via intrinsic catalytic activity, Nat. Commun. 9 (2018) 2920.

[28] P.C. Naha, Y. Liu, G. Hwang, Y. Huang, S. Gubara, V. Jonnakuti, A. Simon-Soro, D. Kim, L. Gao, H. Koo, D.P. Cormode, Dextran-coated iron oxide nanoparticles as biomimetic catalysts for localized and pH-activated biofilm disruption, ACS Nano 13 (2019) 4960–4971.
[29] Y. Zhao, Q. Guo, X. Dai, X. Wei, Y. Yu, X. Chen, C. Li, Z. Cao, X. Zhang, A biomimetic non-antibiotic approach to eradicate drug-resistant infections, Adv. Mater. 31 (2019) 1806024.
[30] Y. Zhao, C. Yu, Y. Yu, X. Wei, X. Duan, X. Dai, X. Zhang, Bioinspired heteromultivalent ligand-decorated nanoplatform for enhanced photothermal and photodynamic therapy of antibiotic-resistant bacterial Pneumonia, ACS Appl. Mater. Interfaces 11 (2019) 39648–39661.
[31] Q. Guo, Y. Wang, L. Zhang, P. Zhang, Y. Yu, Y. Zhang, C. Li, S. Jiang, X. Zhang, In situ real-time tracing of hierarchical targeting nanostructures in drug resistant tumors using diffuse fluorescence tomography, Chem. Sci. 10 (2019) 7878–7886.
[32] A. Galstyan, R. Schiller, U. Dobrindt, Boronic acid functionalized photosensitizers: a strategy to target the surface of bacteria and implement active agents in polymer coatings, Angew. Chem. Int. Ed. 56 (2017) 10362–10366.
[33] Y. Chen, Z. Li, H. Wang, Y. Wang, H. Han, Q. Jin, J. Ji, IR-780 loaded phospholipid mimicking homopolymeric micelles for near-IR imaging and photothermal therapy of pancreatic cancer, ACS Appl. Mater. Interfaces 8 (2016) 6852–6858.
[34] C. Cheng, X. Zhang, Y. Wang, L. Sun, C. Li, Phenylboronic acid-containing block copolymers: synthesis, self-assembly, and application for intracellular delivery of proteins, New J. Chem. 36 (2012) 1413–1421.
[35] S.R.S. Ting, E.H. Min, P.B. Zetterlund, M.H. Stenzel, Controlled/living ab initio emulsion polymerization via a glucose RAFTstab: degradable cross-linked glyco-particles for Concanavalin A/FimH conjugations to cluster E. coli bacteria, Macromolecules 43 (2010) 5211–5221.
[36] Y. Zhao, Z. Lu, X. Dai, X. Wei, Y. Yu, X. Chen, X. Zhang, C. Li, Glycomimetic-conjugated photosensitizer for specific Pseudomonas aeruginosa recognition and targeted photodynamic therapy, Bioconjugate Chem. 29 (2018) 3222–3230.
[37] S. Zhu, M. Niu, H. O'mary, Z. Cui, Targeting of tumor-associated macrophages made possible by PEG-sheddable, mannose-modified nanoparticles, Mol. Pharm. 10 (2013) 3525–3530.
[38] D. Bazile, C. Prud'homme, M. Bassoullet, M. Marlard, G. Spenlehauer, M. Veillard, Stealth me. PEG-PLA nanoparticles avoid uptake by the mononuclear phagocytes system, J. Pharmaceut. Sci. 84 (1995) 493–498.
[39] N. Li, T. Li, C. Hu, X. Lei, Y. Zuo, H. Han, Targeted near-infrared fluorescent turn-on nanoprobe for activatable imaging and effective phototherapy of cancer cells, ACS Appl. Mater. Interfaces 8 (2016) 15013–15023.
[40] M.I. Klein, K.M. Scott-Anne, S. Gregoire, P.L. Rosalen, H. Koo, Molecular approaches for viable bacterial population and transcriptional analyses in a rodent model of dental caries, Mol. Oral. Microbiol. 27 (2012) 350–361.
[41] W.H. Bowen, Rodent model in caries research, Odontology 101 (2013) 9–14.
[42] R.H. Larson, In merits and modifications of scoring rat dental caries by Keyes' method, Spl. Supp. Microbiol. Abstr. (1981) 195–203.
[43] L. Su, Y. Li, Y. Liu, R. Ma, Y. Liu, F. Huang, Y. An, Y. Ren, H. van der Mei, H. Busscher, L. Shi, Antifungal-inbuilt metal-organic-frameworks eradicate Candida albicans biofilms, Adv. Funct. Mater. 30 (2020) 2000537.
[44] Y. Yu, T. Zhang, X. Dai, X. Dai, X. Wei, X. Zhang, C. Li, Therapeutic nanoplatforms with bacteria-specific activation for directional transport of antibiotics, Chem. Commun. 54 (2018) 12754–12757.
[45] Y. Yu, X. Dai, X. Wei, X. Dai, C. Yu, X. Duan, X. Zhang, C. Li, Synthetic fluorescent nanoplatform based on benzoxaborole for broad-spectrum inhibition of bacterial adhesion to host cells, Chem. Mater. 30 (2018) 8795–8803.
[46] G. Achanta, A. Modzelewska, L. Feng, S.R. Khan, P. Huang, A boronic-chalcone derivative exhibits potent anticancer activity through inhibition of the proteasome, Mol. Pharmacol. 70 (2006) 426–433.
[47] J. An, Q. Guo, P. Zhang, A. Sinclair, Y. Zhao, X. Zhang, K. Wu, F. Sun, H.-C. Hung, C. Li, S. Jiang, Hierarchical design of a polymeric nanovehicle for efficient tumor regression and imaging, Nanoscale 8 (2016) 9318–9327.
[48] E. Zhao, Y. Hong, S. Chen, C.W.T. Leung, C.Y.K. Chan, R.T.K. Kwok, J.W.Y. Lam, B. Z. Tang, Highly fluorescent and photostable probe for long-term bacterial viability assay based on aggregation-induced emission, Adv. Healthc. Mater. 3 (2014) 88–96.
[49] H. Zhang, Y. Zhu, Y. Li, X. Qi, J. Yang, H. Qi, Q. Li, Y. Ma, Y. Zhang, X. Zhang, L. Zhang, A bifunctional zwitterion-modified porphyrin for photodynamic nondestructive tooth whitening and biofilm eradication, Adv. Funct. Mater. (2021) 2104799.
[50] Y. Sun, X. Sun, X. Li, W. Li, C. Li, Y. Zhou, L. Wang, B. Dong, A versatile nanocomposite based on nanoceria for antibacterial enhancement and protection from aPDT-aggravated inflammation via modulation of macrophage polarization, Biomaterials 268 (2021) 120614.
[51] X. Sun, J. Sun, Y. Sun, C. Li, J. Fang, T. Zhang, Y. Wan, L. Xu, Y. Zhou, L. Wang, B. Dong, Oxygen self-sufficient nanoplatform for enhanced and selective antibacterial photodynamic therapy against anaerobe-induced periodontal disease, Adv. Funct. Mater. (2021) 2101040.
[52] X. Xu, M. Fan, Z. Yu, Y. Zhao, H. Zhang, J. Wang, M. Wu, F. Sun, X. Xu, C. Ding, J. Li, A removable photothermal antibacterial "warm paste" target for cariogenic bacteria, Chem. Eng. J. 429 (2022) 132491.